Study of the microstructure evolution of alloy structural steel and inhomogeneity effect of the microscale pulsed currents during Current-Assisted Plane Strain Compressions by modeling a novel Cellular Automata Method

Can Chen[1, 3], Qinxiang Xia[1, 3, *], Haoyang Zhou[1, 3], Jie Zhao[2], Yi Qin[2, *], Gangfeng Xiao[1, 3]

[1]School of Mechanical and Automotive Engineering, South China University of Technology, Guangzhou, 510641, People's Republic of China.

[2]Centre for Precision Manufacturing, DMEM, University of Strathclyde, Glasgow, G1 1XQ, United Kingdom

[3]Guangdong Provincial Key Laboratory of Precision Equipment and Manufacturing Technology, South China University of Technology, Guangzhou, 510641, People's Republic of China.

[*]Corresponding Authors: meqxxia@scut.edu.cn (Q. X. Xia); qin.yi@strath.ac.uk (Y. Qin)

Abstract

The current-assisted forming process is considered to be a novel process that utilizes the electroplasticity effect to reduce the deformation resistance of difficult-to-deform metals and to refine the grain size while improving the mechanical properties of the part. However, the lack of understanding of the mechanisms by which pulsed current affects grain refinement still makes it difficult to experimentally develop analytical or empirical models of the relationship between grain size, pulse current parameters, and deformation amount. It will seriously hinder the further development and application of the current-assisted forming process. To reveal the mechanism of grain refinement coupling with electroplasticity, a series of Electron Back Scattering Diffraction observation tests were carried out after current-assisted plane strain compressions. The results show that the grain orientation spread value of the pulse current condition is lower than that of the non-current condition, while the refined grain area percentage is higher than that of the non-current condition. Based on the microstructure observation results, a cellular automata model for grain refinement is proposed. This consists of a dislocation density evolution, sub-grains generation, grain fragmentation, and a grain orientation rotation algorithm. To study the electroplasticity of the grain refinement process, the cellular automata model is also embedded with a finite difference numerical algorithm for solving the microscopic current density distribution of the model. The cellular automata model simulation results show that the error of grain size accuracy of this cellular automata model under non-current and pulse current conditions is 10.48 % and 8.55 %, respectively. It shows that the model can accurately characterize the grain refinement behavior of the current-assisted plane strain compression. The simulation results reveal the deep mechanism of pulsed current promotion on grain refinement, i.e., an inhomogeneous microstructure leads to uneven distribution of pulse current density. The inhomogeneous current distribution will further increase the grain refinement rate in the coarse-grained regions, thus increasing the proportion of the refined grain regions in the microstructure and leading to a relatively more homogeneous microstructure under pulse current conditions. The cellular automata model accurately reveals the mechanism of electroplasticity on the grain refinement. The model will serve as a crucial theoretical reference in designing current-assisted forming process routes to ensure excellent microstructure and properties in manufactured parts. It will enhance the widespread utilization of current-assisted forming process.

Keywords Cellular Automata; Alloy structural steel; Grain refinement; Electroplasticity; Current-assisted Metal Forming

1. Introduction

The chemical elements and microstructure will determine the mechanical and physical properties of the metal. Hence, the regulation of microstructure is one of the essential ways to improve the service performance of the material. For example, to achieve the desired strength and toughness properties, the alloy structural steel 30CrMnSiA, as a difficult-to-deform metal, commonly used to manufacture structural components, must be a fine microstructure obtained through a hot deformation process/hot treatment. This traditional manufacturing process not only has a long production cycle, but also leads to high energy consumption. Grain refinement via severe plastic deformation processes at room temperature is an effective way to achieve green manufacturing in the future [1–3]. However, the high strength and work hardening index of 30CrMnSiA requires the deformation force to be much higher at room temperature than that of the thermal forming processes. The current-assisted forming process (CAFS) is considered a novel manufacturing method that can effectively reduce the deformation resistance and achieve a grain-refined microstructure at room or warm temperature conditions [4]. Many research reports have previously showed that current-assisted forming technology can obtain a more refined microstructure and have explained the mechanism [5–7]. It can reduce the recrystallization temperature and promote nucleation, etc.[8–10]. However, the academic community has not fully understood the grain refinement mechanism caused by the electroplastic effect. Because of the experimental methods employed, the microstructure characterization remains complicated to visualize. Other macroscopic models can only obtain overall microstructure parameters such as average grain size [11,12], which cannot accurately reflect local details of the metal microstructure with random properties. Therefore, a numerical microstructure evolution model incorporating electroplasticity is crucial to the shaped-microstructure integrated control aspects of current-assisted forming. It is also an important prerequisite for predicting the microstructure and mechanical properties during CAFS.

There are many numerical models for the microstructural evolution during the deformation process, such as Monte Carlo [13], phase field [14], or cellular automata (CA) [15–17]. The CA model is one of the most commonly used methods for characterizing grain refinement during large plastic deformation processes, such as rolling [18], forging [19], and power spinning [20]. It is widely accepted that the grain refinement process during hot deformation should consist of three components: continuous dynamic recrystallization (cDRX), discontinuous dynamic recrystallization (dDRX), and geometric dynamic recrystallization (gDRX) [21]. For example, Liu L et al. established a cDRX-CA model to predict the microstructural evolution of Al2219 alloy under high-temperature conditions, which divides the cDRX process into three stages: dislocation density evolution, sub-grain nucleation, and sub-grain boundary migration [22]. However, since the temperature is far from the dynamic recrystallization (DRX) temperature conditions (T>0.6Tm) during the pulse current-assisted warm-forming process [23], the dislocation-density multiplication induced by strain is regarded as the only grain refinement mechanism under room/warm temperature conditions. The mechanism suggests that a subgrain structure will be generated, rotated, and transformed into high-angle grain boundaries within the initial microstructure as the dislocation density accumulates [24]. Zhang J and Liu G X et al. constructed a CA model for grain refinement and investigated the microstructure evolution of the workpiece surface during cutting OFHC Cu and Ti-6Al-4V, respectively [25,26]. It was found that the strain-generated increase in dislocation density has a dominant role in the grain refinement process. In addition, Dmytro S. Svyetlichnyy et al. developed a novel Frontal CA model to predict the changes in morphology, grain size, and misorientation during severe plastic deformation of AISI 304L steel [2]. So far, there are only a limited number of

reports on the grain refinement modeling during the current-assisted process. Zhao J Y et al. investigated the local current density distribution based on the CA model. They showed that the high current density near the grain boundary nodes has the potential to generate local Joule heat [27]. This study just constructed a static model and did not involve the dynamic evolution process of the microstructure. In summary, it is still very challenging to characterize the mechanisms of electrophysical effects within the framework of CA models.

In previous work, the current-assisted plane strain compression (CAPSC) test was employed to investigate the deformation behavior of 30CrMnSiA, and a dislocation-density evolution constitutive model was constructed under electroplasticity [28]. This study analyzes the Electron Back Scattering Diffraction (EBSD) test results following the CAPSC test to study the impact of electroplasticity on the grain refinement process. A CA model is developed to accurately characterize the microstructural evolution during the CAPSC process, which incorporates computational mathematical models of dislocation density evolution, sub-grain generation, and orientation angle rotation induced by pulse current. The CA model requires finite element (FE) model results as input boundary information for deformation. Finally, the mechanism of increasing strain and inhomogeneous pulse current density in the grain refinement process is discussed based on the simulation results. This result can provide a practical numerical tool for precisely controlling microstructure properties during CAFS, such as current-assisted multi-pass spinning or rolling in the future.

2 Experiment and FE modeling of CAPSC

2.1 Experimental procedures

The test material is 30CrMnSiA, composed of equiaxial α-ferrite and lamellar pearlite after annealing treatment, and is shown in Figure 1(a) obtained through the optical and Scanning Electron Microscope (SEM) observation experiments. Figure 1(b) shows the statistical results of grain size distribution for Figure 1(a) that conforms to a Gaussian distribution. The average grain size (D_{ave}) of the microstructure is 14.3 μm, and more than 80% of the grain size is in the range of 5 -25 μm. Table 1 shows the chemical composition of the material. The CAPSC test device is shown in Figure 2(a). The original dimensions of the compression specimen were 20 mm × 15 mm × 2 mm (length × width× thickness). During the tests, a high-frequency pulsed current with a voltage of 5 V and a frequency of 100 Hz was accessed through electrodes at both sides of the specimen. The input current conditions were set to 0 A/mm^2 and 30 A/mm^2, representing the non-current condition (NC) and pulsed current condition (PC). The selected basis for the pulse current parameters can be found in the literature [28]. The universal testing machine applied load to the specimen at a strain rate of 0.01 s^{-1}. The experiment was stopped when the deformation strain ε_p reached 0.4, 0.8, and 1.2, respectively, and the center area of the deformed sample was collected as the sample for the EBSD experiment, as shown in Figure 2(b). The experimental step of EBSD was selected as 0.12 μm. The EBSD data were analyzed using the MATLAB-based MTEX toolbox and Channel 5.

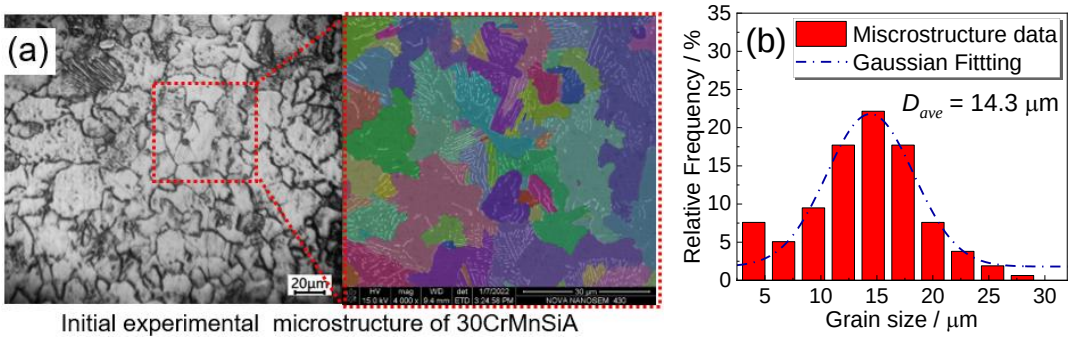

Fig.1. The initial microstructure of 30CrMnSiA: (a) Optical & SEM image and (b) grain size distribution

Table 1 Chemical components of 30CrMnSiA alloy structural steel (in wt%)

Element	C	Si	Mn	Cr	S	P	Ni	Cu	Fe
Content	0.28-0.34	0.90-1.20	0.80-1.10	0.80-1.10	≤0.025	≤0.025	≤0.030	≤0.025	Balanced

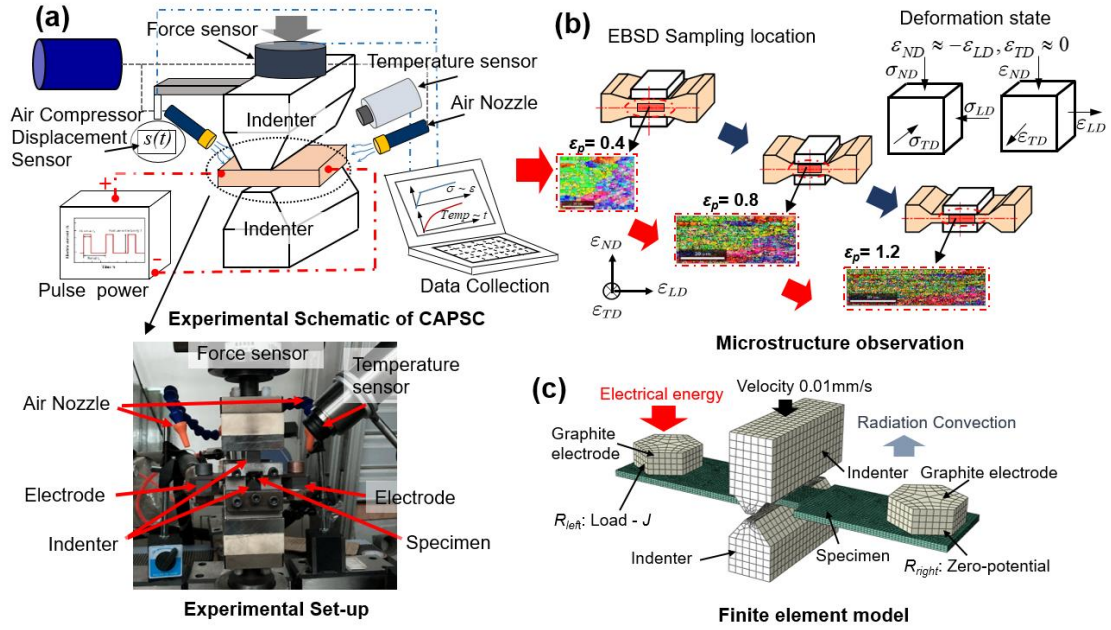

Fig. 2. Schematic diagram and FE model of CAPSC test and EBSD test: (a) Equipment of CAPSC process, (b) Sample of EBSD observation and (c) finite element modelling

2.2 FE modelling and CA model boundary

Since the grain refinement process is related to the strain and the CA model is a time-discrete simulation model, it is necessary to determine the strain and pulse current density versus time as an input boundary condition for the CA model during deformation. Finite element modeling is a crucial technique to obtain the deformation history of local fine regions. According to the dislocation constitutive model described later in section 4.1, an ABAQUS subroutine to simulate the plastic deformation behavior of 30CrMnSiA was developed for the CAPSC deformation. Figure 2 (c) presents the parts, boundary conditions, and mesh used in the FE model. The geometric dimension of the parts could be referred to in the published literature [29]. The model employed an 8-node brick, tri-linear displacement, electric potential, and temperature element (Q3D8 in ABAQUS). The total number of nodes and elements were 14424 and 11923, respectively. The grid size of the deformation zone was locally refined to 0.4 mm to achieve an accurate simulation of severe plastic deformation. Figure 2(c) also outlines the boundary

conditions. The upper indenter velocity was set to 0.01 mm·s^{-1}, and two electrodes supplied the specimen with pulsed current and zero potential, respectively. All surfaces of the parts were set to a film condition of 25×10^{-6} W/(mm^2·K) in the ABAQUS software to simulate the heat transfer coefficient under the force air-cooling conditions [30]. The parts are all constructed from steel, with a surface emissivity value of 0.65 to simulate the radiative heat dissipation process [31]. Table 2 lists the thermodynamic coefficients and thermal-electrical properties of the materials employed [32,33]. The transient coupled thermo-electric-structural solver was used to solve this model.

Figure 3 shows the simulation results of the FE model under PC conditions. The results show that the average principal strain of the deformation zone is ε_{LD} = 1.225, ε_{ND} = -1.119, and ε_{TD} = -0.0967 ≈ 0, which is basically consistent with the assumption of plane strain compression. As shown in Figure 4(a), the constructed FE model is verified by comparing the deformation forces measured by the FE model and the universal testing machine, and the results show a high level of accuracy with a maximum relative error of the data of 9.31%. Additionally, Figure 4(b) presents the maximum temperature history of the specimen as determined by both the FE model and the CAPSC test with a consistent trend. It is worth noting that the temperature is stable when powered up to 120 seconds. The maximum temperature error between the model and the test at the stable stage is 8.21%. As shown in Figure 4(c), the strain-displacement and equivalent pulse current density-displacement histories of the specimen center cell are used as the macroscopic deformation boundary conditions driving the evolution of the CA model.

Table 2 Thermal & electrical parameters of 30CrMnSiA

Temperature /℃	100	150	200	250	300
Heat conduction coefficient /(W·mm^{-1}·K^{-1})	0.0305	0.0299	0.0293	0.0285	0.0276
Specific heat /(J/Kg^{-1}·K^{-1})	503	505	511	516	523
Electrical conductivity (10^3·Ω^{-1}·mm^{-1})	3.69	3.25	2.92	2.67	2.41

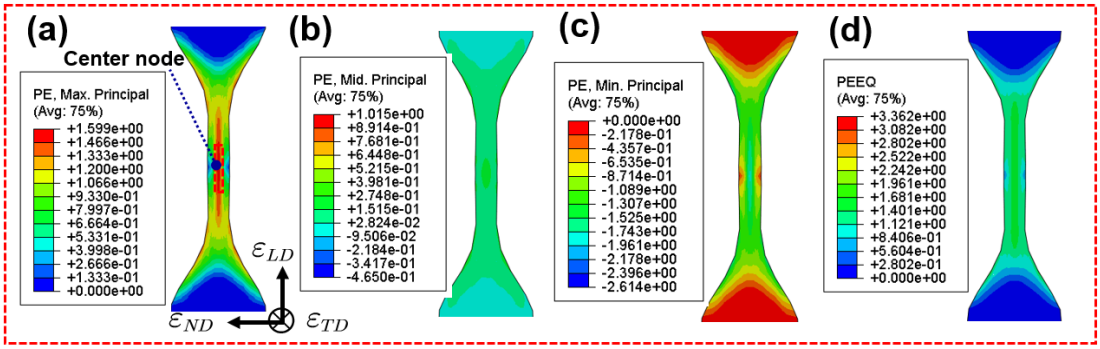

Fig. 3. Simulation result of FE model under PC condition for the deformation zone: (a) first principal strain, (b) second principal strain, (c) third principal strain and (d) equivalent strain

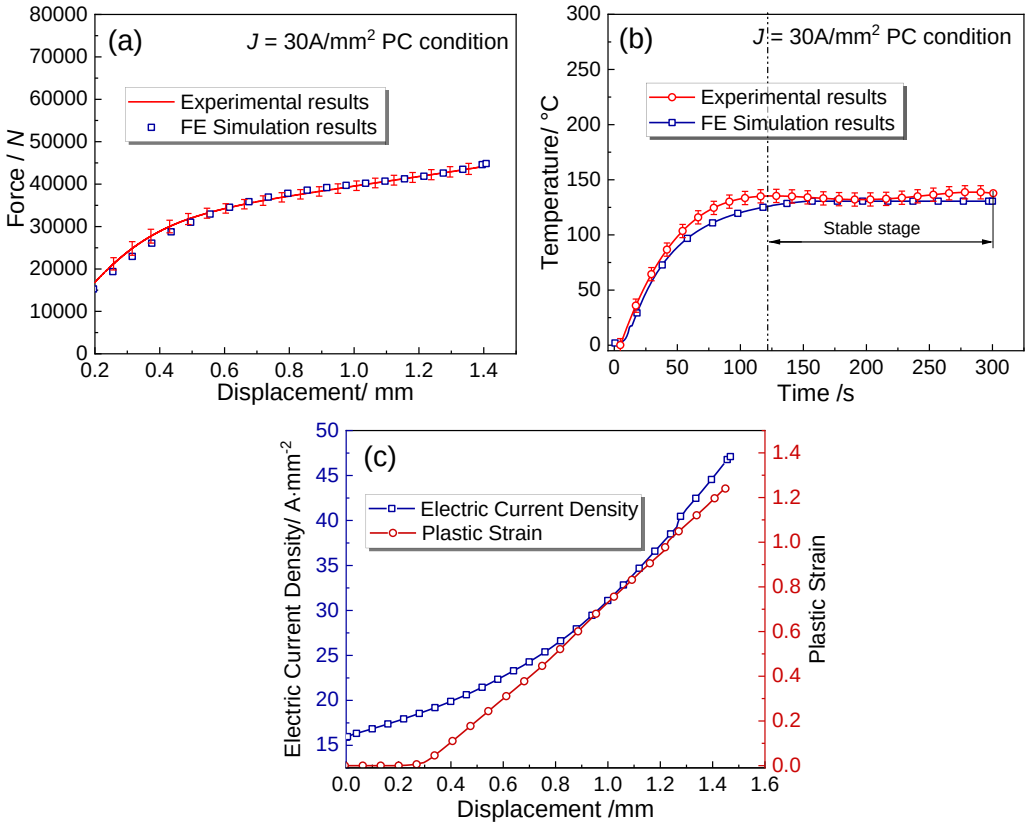

Fig. 4. Result and variable output of the FE simulation: model accuracy validation with (a) force history, (b) temperature history and (c) variation of equivalent strain and current density at deformation zone

3 Experimental results and discussion

Figure 5 shows the microstructure under different strains and pulse current conditions, in which the green line represents low-angle grain boundaries (LAGBs, 2° < misorientation < 15°) and the black line represents high-angle grain boundaries (HAGBs, misorientation > 15°) [34]. The results show that grain refinement was produced during CAPSC under NC and PC conditions. The microstructure at low strain levels (ε_p = 0.4) and moderate strain levels (ε_p = 0.8) shows varying degrees of deformation; that is, it gradually changes from equiaxed grains to compression along the *ND* direction and elongation along the *LD* direction. As shown in Figure 5(a)-(b) and (d)-(e) within the red-circled region, some fine grains appear near the boundary of the coarse grains, producing similar orientation difference gradients and chain-like structures. When deformed to a high strain state (ε_p=1.2), equiaxed refined grains have occupied most of the area, and the compressive deformation microstructure is almost invisible. For low/medium strain inhomogeneous structures, the number-based average grain size tends to be significantly affected by the number of refined grains. In contrast, the equivalent grain size calculates the average value based on the area percentage, which substantially reduces the influence of microstructure inhomogeneity and grain number on the grain size evaluation. This paper uses the equivalent grain size $\bar{D}_e$ as a parameter to measure the degree of microstructure grain refinement with the following equation [35]:

$$D_{eq} = \sum_{i=1}^{N_g} \frac{A_i}{A} \cdot \sqrt{\frac{4 \cdot n_i \cdot l_0^2}{\pi}} \tag{1}$$

where A_i is the grain area of the i^{th} grain, and A is the area of the entire EBSD observation region. n_i is the number of pixels in the i^{th} grain, and N_g is the total number of grains. l_0 is the scan step size of the EBSD test. The equivalent grain sizes under NC conditions are 5.30 μm, 4.16 μm and 1.44 μm, while the equivalent grain sizes under PC conditions are 4.19 μm, 2.97 μm and 1.24 μm, respectively. This shows that the grain size of the microstructure was getting finer with the increase of strain. Moreover, the electroplastic effect caused by the pulse current promotes the grain refinement process, making the equivalent grain size smaller at the same strain. The equivalent grain size under pulsed current was reduced by 13.9 % at ε_p = 1.2. Comparison of Figure 5(c) and 5(f) show that the microstructure obtained in the NC condition contains more coarse grains, as shown by the blue circle. On the other hand, the microstructure obtained in the PC condition is also more homogeneous, and there are no noticeable coarse microstructural components.

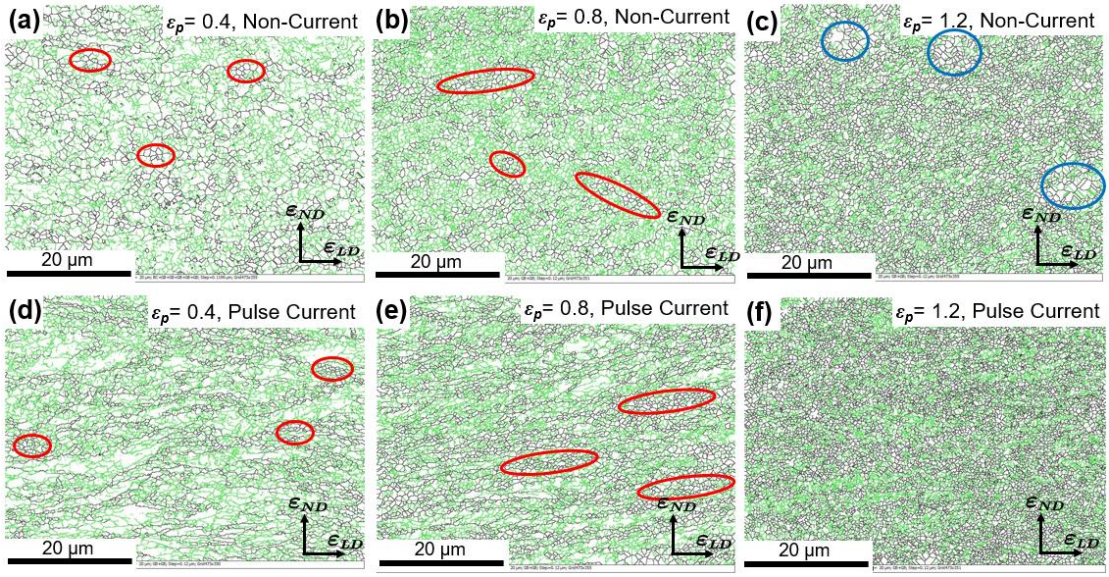

Fig. 5. The HAGB and LAGB maps of microstructure under different strain and pulse current conditions. (a) ε_p = 0.4 under NC, (b) ε_p = 0.8 under NC, (c) ε_p = 1.2 under NC, (d) ε_p = 0.4 under PC, (e) ε_p = 0.8 under PC and (f) ε_p = 1.2 under PC

Figure 6 shows the grain orientation spread (GOS) at different strain and pulse current conditions, representing the average misorientation angles for each grain. As the strain increases, the GOS maps show that the deformed grains (the orange/red area in the figures) gradually decrease, while the refined grains (the blue/green area in the figures) gradually increase. The GOS value can represent the storage energy at the grain interior caused by deformation. Specifically, those grains with GOS < 5° represent less deformation storage energy, indicating that they belong to the grains that have undergone refinement (GOS < 2°) or are currently undergoing refinement (2° < GOS < 5°). Based on the definition, the blue and dark green grains in Figure 6 represent the grains that have undergone or are currently undergoing refinement, respectively. The area ratio of these grains can characterize the degree of grain refinement in the microstructure [36]. Figure 7 shows the statistical results of equivalent GOS and the refine grain area percentage (GOS < 5°, including blue and dark green) obtained from Figure 6. There are more blue grains in Figure 6(a) than in Figure 6(d), while more dark green refined grains are present in Figure 6(d). This phenomenon is because more grains are converted to soft phases under PC conditions, resulting in more grains undergoing uniform plastic deformation [37]. It means that under PC conditions, most of the refined grains are still in grain refinement (dark green, 2° < GOS < 5°). Under the minor deformation of ε_p = 0.4 and PC conditions, more grains are involved in plastic deformation, making the amount of

deformation allocated to each grain insufficient for it to achieve grain refinement ultimately. In contrast, the plastic deformation under the NC condition is inhomogeneous and occurs in only a few grains. Thus, these grains have a higher refinement completion (blue, GOS ≈ 0°). The difference in total refined grain area (including blue and dark green grains) between the NC and PC conditions was slight at $\varepsilon_p = 0.4$. The equivalent GOS difference is only 2.8 %. The difference in refined grain area is 1.72 %, which is almost insignificant, indicating that the impact of pulse current at low strain levels is negligible. However, at $\varepsilon_p = 1.2$, the equivalent GOS in the NC condition decreases from 5.24 ° to 4.11 ° in the PC condition with a decrease of 21.56 %, while the percentage of the area of refined grains increases from 57.36 % to 72.89 % with the increase of 15.53 %. This change shows that as the strain increases, the degree of grain refinement becomes higher, and the influence of the pulse current becomes more obvious.

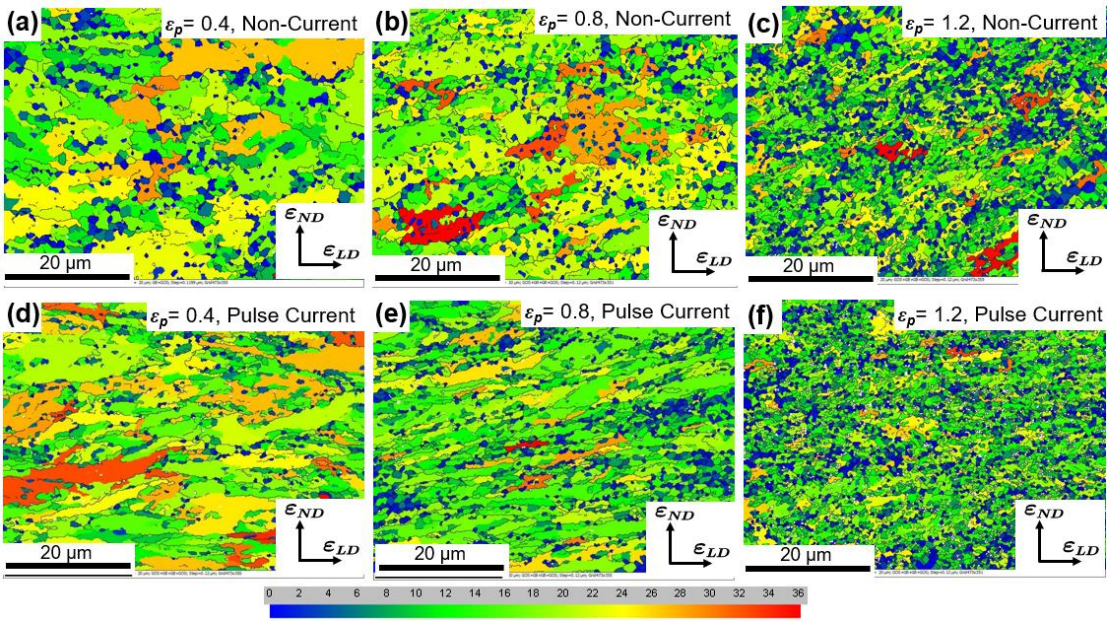

Fig. 6. GOS maps of the EBSD sample under different conditions. (a) $\varepsilon_p = 0.4$ under NC, (b) $\varepsilon_p = 0.8$ under NC, (c) $\varepsilon_p = 1.2$ under NC, (d) $\varepsilon_p = 0.4$ under PC, (e) $\varepsilon_p = 0.8$ under PC and (f) $\varepsilon_p = 1.2$ under PC

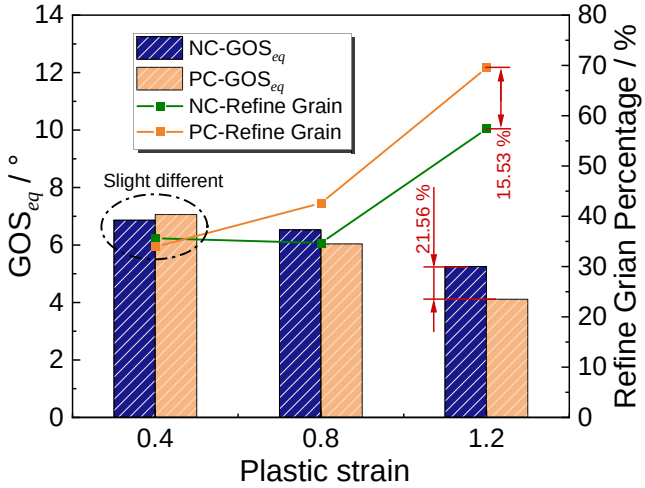

Fig. 7. Statistical value based on the EBSD test for various strain under NC and PC conditions: (a) GOS average and (b) refine grain percentage

4 Physical basis of grain refinement CA model subject to pulse current

Since the temperature under the experimental conditions of CAPSC is insufficient to satisfy the thermal activation conditions [28], generating microstructural dislocations, accumulation, and aggregation are the main driving forces leading to grain refinement [3]. This grain refinement mechanism is sometimes called strain-induced grain refinement or fragmentation [38,39]. The process is summarized in Figure 8. The accumulation of dislocations forms dislocation cells and dislocation density lines, representing the formation of localized misorientation. As strain increases, the microstructure with high storage energy becomes unstable and then splits to LAGBs once the critical dislocation density value is reached. At last, with the further accumulation of dislocations, the misorientation between sub-grains exceeds 15 ° to complete the grain refinement process. It can be seen that the grain refinement mechanism involves four sections, namely, the accumulation of dislocation density, grain fragmentation, sub-grain generation, grain orientation rotation, etc., which will be described in the subsequent sections.

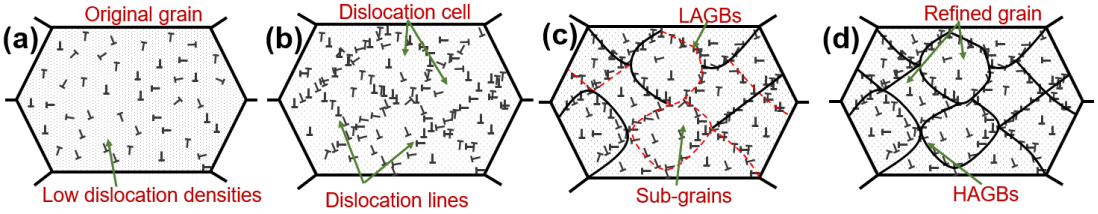

Fig. 8. Schematic diagram of grain refinement process based on (a) dislocation density accumulation, (b) dislocation cell and line generation and formation of (c) LAGBs and (d) HAGBs

4.1 Dislocation density evolution model

During electrical current-assisted severe plastic deformation of 30CrMnSiA, the rate of dislocation density accumulation mainly consisted of three parts: (1) the formation and accumulation rate of dislocation density caused by plastic deformation. (2) the reduction of dislocation due to dislocation cell formation and conversion to sub-grain boundaries. (3) the dislocation annihilation rate caused by the elimination and rearrangement of the dislocation. Therefore, the traditional K-M model that considers grain refinement phenomenon can be modified as presented, as described following:

$$\dot{\rho}_i = \rho_i^{1+} - \rho_i^{1-} - \rho_i^{2-} \tag{2}$$

where, $\dot{\rho}_i$ is the average dislocation density increasing rate, ρ_i^{1+} is the storage rate for the formation and accumulation of the dislocation density, ρ_i^{1-} is the reduction rate of the dislocation density due to sub-grain formation, and ρ_i^{2-} represents the rate of dislocation annihilation resulting from elimination and rearrangement. The subscript i denotes the parameter value of the i^{th} cell in the CA model. According to our previous study [28], the average dislocation density is characterized as a weighted average of dislocation density in grain cells ρ_c and dislocation density in grain boundaries ρ_w, which can be calculated by [11]:

$$\frac{d\rho_c}{d\gamma} = \alpha^* \frac{1}{\sqrt{3}b}\sqrt{\rho_{ws}+\rho_{wg}}\dot{\gamma} - \beta^* \frac{6}{bd_{ave}(1-f)^{1/3}}\dot{\gamma} - k_0\left(\frac{\dot{\gamma}}{\dot{\gamma}_0}\right)^{-1/n}\rho_c\dot{\gamma} \tag{3}$$

$$\frac{d\rho_{ws}}{d\gamma} = \beta^* \frac{\sqrt{3}(1-f)}{fb}\sqrt{\rho_{ws}+\rho_{wg}}\dot{\gamma} + \beta^* \frac{6(1-f)^{2/3}}{bd_{ave}f}\dot{\gamma} - k_0\left(\frac{\dot{\gamma}}{\dot{\gamma}_0}\right)^{-1/n}\rho_{ws}\dot{\gamma} \tag{4}$$

where, ρ_w is the total grain wall dislocation density, which consists of the statistical dislocation density (ρ_{ws}) and the geometrically necessary density (ρ_{wg}). α^*, β^*, k_0, n, and $\dot{\gamma}_0$ are material constants that

control the rates of dislocation evolution. b is the Burgers vector (2.86×10^{-10} m). The resolved shear rate $\dot{\gamma}$ can be determined using the strain rate $\dot{\varepsilon}$ and the Taylor factor M, i.e., $\dot{\gamma}=M\dot{\varepsilon}$, as described in [40].

The CAPSC tests described in Section 2.1 used a strain rate of 0.01 s^{-1}, and the material Taylor factor M is 3.06, resulting in a resolved shear strain rate $\dot{\gamma}$ of 0.0306 for the model. γ is the resolved shear strain and also has a similar relationship, i.e. $\gamma=M\varepsilon$. ε are determined by FE model results, such as Figure 4(c).The volume fraction of the grain wall f, geometrically necessary density ρ_{wg}, and average grain size d_{ave} can be calculated as follows [41]:

$$f = f_\infty + (f_0 - f_\infty)\exp\left(\frac{\gamma}{\eta}\right) \tag{5}$$

$$\frac{d\rho_{wg}}{d\gamma} = \xi\beta^* \cdot \frac{6(1-f)^{2/3}}{bd_{ave}f}\dot{\gamma} \tag{6}$$

$$d_{ave} = \frac{K}{\sqrt{\rho_{tot}}}, where \quad \rho_{tot} = f\rho_w + (1-f)\rho_c \tag{7}$$

where K is a material constant, f_0 and f_∞ are the initial and saturation values of f, respectively; α^* and β^* is usually taken as a constant to represent the interaction among distinct dislocations during the evolution of microstructure [11,42]; f_0 and f_∞ are material constants, related to the state and properties of the material [43]. $\dot{\gamma}_0$ is called the reference strain rate, and its magnitude is closely related to the material properties [40,44,45]. The material parameters and constants used for the dislocation density evolution model are listed in Table 3, which are obtained by fitting the stress-strain curve using the Levenberg-Marquardt algorithm [28]. The precision of the final model fitting is as shown in Figure 9. The correlation coefficient(R) and the average relative error ($AARE$) of the stress by the dislocation evolution model (equation (3) - (7)) is 0.974 and 4.56%, respectively, which shows that the material parameters used have high reliability.

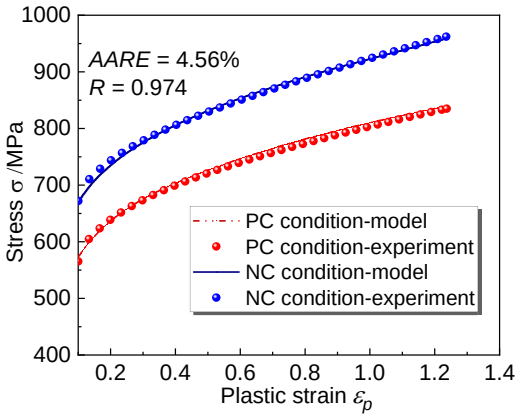

Fig. 9. Prediction accuracy of dislocation density evolution model under PC and NC conditions

The term $k_0(\dot{\gamma}/\dot{\gamma}_0)^{-1/n}$ influencing the rate of dislocation density annihilation is generally considered to be a function of both the current density (J) and temperature (T)[32,46]. n is a coefficient representing the rate sensitivity of the material, which is used to characterize the influence of the current-induced deformation temperature [47]. In these research, the temperature T was close to or exceeded the recrystallization temperature (~$0.5T_m$) [48,49]. A comparison of the thermal compression and the CAPSC tests showed that the temperature rise effect of 30CrMnSiA is low (~100°C) at low current

density, which is much less than $0.5T_m$ [28]. Therefore, it can be assumed that the influence of the thermal softening on the material properties can be negligible under the pulse current parameter of J = 30A/mm^2. The properties of 30CrMnSiA under the test conditions of J = 30A/mm^2 is similar to those at room temperature[28], and it can be referred to as a strain-rate insensitive material. Therefore, the material coefficient n associated with the assumption of rate sensitivity in the equation (3) - (4) is set to a constant value. Furthermore, the influence of pulse current on the dislocation density annihilation rate can be introduced by assuming the coefficient k_0 as a function of the T and J [50]. Therefore, k_0 in equation (3) - (4) is assumed to be a function of the J due to the influence of temperature is neglected. In addition, the coefficient η in equation (5) is assumed to be a function of J because of the grain refinement process being influenced by the pulse current also based on the CAPSC result [28]. The parameter evolution functions of k_0 and η for the current density J are shown below. It is noteworthy that here, the mechanism by which the electroplasticity effect affects the evolution of the microstructure is incorporated into the CA modeling framework, i.e., the material parameters of the evolution equation in each cell will vary based on the magnitude of the pulsed current density.

Table 3 Material parameters of dislocation density evolution model for 30CrMnSiA [28]

Parameter	α^*	β^*	n	$\dot{\gamma}$	f_0	f_∞
Value	252.4	1.47e-5	87273.67	1.9e7	0.29	0.077

$$k_0 = 11.66 - 3.899\exp\left(-J/0.1882\right) \tag{8}$$

$$\eta = 0.4018 + 0.0462\exp\left(-J/0.1634\right) \tag{9}$$

4.2 Sub-grain formation model

When the dislocation density accumulates to a critical value, LAGBs are formed within the grain. Based on the classical theory of the dislocation density, the relationship between the misorientation and dislocation density satisfies the following equation [26]:

$$\theta \propto \arctan\left(b\sqrt{\rho}\right) \approx rb\sqrt{\rho} \tag{10}$$

where, r is a material constant set to 10 for 30CrMnSiA, and new sub-grain boundaries are considered to be formed when the misorientation reaches a critical value (θ_0 = 2°) [51]. The critical dislocation density for the annealed carbon steel 30CrMnSiA can be calculated as follows:

$$\rho_{critical} = \left(\frac{2\pi\theta_0}{180b}\right)^2 \tag{11}$$

Once the average dislocation density of the coarse grain reaches the critical value of Eq. (10), the coarse grain will split into a plurality of sub-grains. According to Liu G. X et al.[26], the stable grain boundary angle is 120°, so the grain will split equally into three sub-grains to minimize the grain boundary energy of the newly formed sub-grains in their CA model (Figure 10(a)). Toth et al. propose that the lattice curvature near grain boundaries and center is not uniform due to the boundary constraints [52,53]. This lattice curvature theory suggests that the grain will be refined to 9 sub-grains during deformation, as shown in Figure 10(b). The grain refinement processes studied above are all deterministic processes. However, the refinement criterion for each grain in this study was randomized. Several recent studies provide some EBSD tests to show that the smaller the grain size, the more difficult it is to achieve grain refinement [25,26]. The probability P_n of a coarse grain being refined into n sub-grains will be

expressed as a power function of grain size, as expressed below:

$$P_n = c\, d_n^2 / d_{ini}^2 \tag{12}$$

where, the constant c is determined as 0.5 for the grain fragmentation process [25]. d_n represents the sub-grain size after refinement, while d_{ini} represents the current grain size. However, the topological deformation of grains caused by plastic deformation leads to forming elliptical grain shapes, as described in Section 5.2. Therefore, d_n and d_{ini} must be estimated using the equivalent grain diameter d_{eq} [54]. The physical meaning of the d_{eq} is the diameter of a circle having the same area as the irregular grain shape, which is expressed as $d_{eq}=\sqrt{4 \cdot n_i \cdot l_0^{\,2} / \pi}$. The significance of n_i and l_0 is similar to that of equation (1), which is the number of the CA cells in a grain and the size of each CA cell, respectively. The equation (12) shows that the probability of refinement into that number of sub-grains is proportional to the relative diameter square of the refined grains. The model sets the lowest sub-grain refinement number to 3, representing the highest probability of the grain splitting into three sub-grains, making the grain splitting model used in this study also consistent with the classical principle of lowest grain boundary energy. Throughout each iteration of the model, the dislocation density value of the cell increases incrementally following the model detailed in Section 4.1. When the average value of dislocation density within a grain exceeds the critical dislocation density value described in equation (11), a grain refinement process initiates, as showed in Figure 10. The quantity of subgrains post-refinement results from a stochastic process, with its probability governed by equation (12). Each generated subgrain is randomly assigned a set of grain orientations (φ_1^{new}, ψ^{new}, φ_2^{new}) with a misorientation θ_0 of 2° from the old orientations (φ_1^{old}, ψ^{old}, φ_2^{old}), where the formula for the misorientation can be found in Reference [55].

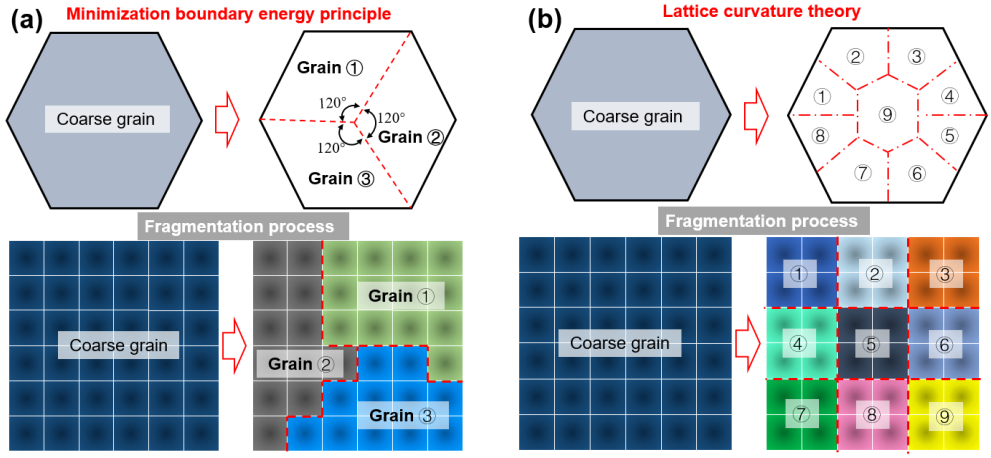

Fig. 10. Status transformation diagram of grain refinement in CA method: (a) Minimization of boundary principle and (b) lattice curvature theory

4.3 Grain rotation mechanism caused by plastic deformation and pulse current

According to the grain refinement mechanism described in Figure 8, the sub-grains at the grain interior will continue to rotate as the strain increases, making the misorientation increase continuously. Figure 11 shows the rotation of polycrystalline materials consisting of plastic spin Ω^p and lattice spin components Ω^e [56]:

$$\Omega = \Omega^e + \Omega^p \tag{13}$$

Since the specimen does not rotate during deformation (Ω = 0), the lattice orientation of each cell must

be changed to offset the plastic spin. The spin rate is related to the activated slip system and the strain rate, i.e.:

$$\Omega(i,j)^e = -\Omega(i,j)^p = -\frac{1}{2}\sum_{\alpha=1}^{n}\left(m(i,j)^\alpha \otimes n(i,j)^\alpha - n(i,j)^\alpha \otimes m(i,j)^\alpha\right)\cdot\dot{\gamma}^\alpha \tag{14}$$

where, $\dot{\gamma}^\alpha$ is the shear strain rate of the α^{th} slip system. m^α and n^α are the unit vectors that denote the slip direction and the normal direction of the slip plane, respectively. According to equation (14), the rotation of the crystal depends not only on the crystal orientation but also on the plastic deformation magnitude. Unfortunately, fully characterizing equation (14) within the CA model remains challenging. Because the spatial coordinates of the cell in the CA model are constant, it is impossible to capture the spatial rotation angle of each material point, as in the case of the crystal plasticity finite element algorithm. Thus, the grain rotation model is simplified: for each deformation increment in the model, an incremental angle ($\Delta\varphi_1$, $\Delta\varphi_2$, $\Delta\varphi_2$) is independently added to each orientation angle component (φ_1, ψ, φ_2) of the cell, resulting in updated orientation angles ($\varphi_1+\Delta\varphi_1$, $\psi+\Delta\varphi_2$, $\varphi_2+\Delta\varphi_2$). The set of cells belonging to the same grain has a consistent orientation angle increment. Considering the calculation efficiency of the CA model and its stochastic characteristics, this article refers to the literature [1]. The rotational direction and rotation of the subgrains will be characterized with a stochastic model, as shown in equation (15) below:

$$\Delta\varphi_i = \theta_0 \cdot r_i \cdot \dot{\varepsilon} \cdot \Delta t, \qquad where \;\; i = 1,2,3 \tag{15}$$

where θ_0 represents the rotation factor, which is equal to 0.5-2.0° for steel material 30CrMnSiA [57], r_i represents a random number in the range [-1,1] to reflect the randomness of the grain rotation direction and value. The subscript i represents each component of the orientation angle, i.e., i = 1, 2, 3. Δt and $\dot{\varepsilon}$ are the time increments and strain rate of each simulation step, respectively. $\Delta\varphi$ represents the increment of the three Euler angles of the cell as a basic state.

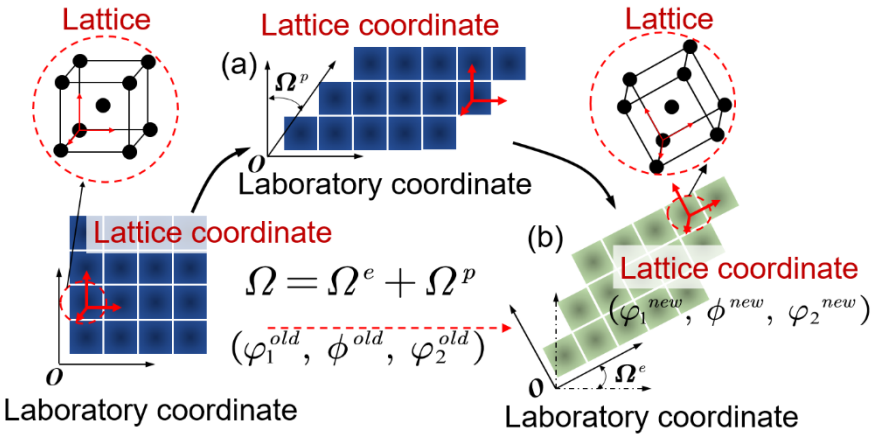

Fig. 11. Schematic of the decomposition of rotation rate Ω into the (a) plastic slip and (b) rigid lattice spin based on the crystal theory

In addition to the grain rotation caused by plastic deformation, the high energy input can cause additional rotational increments in misorientation. According to Daudi Waryoba and co-workers [58], molecular dynamics show that grain rotation does occur during the pulse current annealing treatment. During the grain rotation, the atoms near the grain boundaries are rearranged to reduce dislocation defects and decrease the dislocation energy of the microstructure. Zhao and Ren et al. believe that as the current tends to avoid areas of high resistance, the current density in the microstructure is not uniformly

distributed, making the electric field imbalance between adjacent grains an additional driving force for grain rotation [27,59]. The grain rotation increments can be expressed as [6]:

$$\dot{\varphi}(J)=\frac{8\Omega\cdot\delta\cdot D}{k\cdot T\cdot L^2}\left(\frac{\pi Gb}{1-v}+Z^*e\rho_e JN\right) \tag{16}$$

$$D_i=D_0\exp\left(-Q/RT_i\right) \tag{17}$$

where the first term of the rotation rate is related to the thermal activation Q, and the second is related to the non-thermal effect (electron wind effect), which is proportional to the current density J. Ω is atomic volume. δ is grain boundary thickness. D represents the lattice diffusion coefficient that can be calculated as a function of the Arrhenius equation, as shown in equation (17). G and v are material parameters of the shear modulus and Poisson ratio, respectively. k is the Boltzmann constant. L corresponds to the length of the grain boundary segment, which is equivalent to half of the given grain diameter, represented by $d/2$. Z^* is the effective valence number, ρ_e is the electrical resistivity, and e is the electron charge. N is the atomic density. R and D_0 are the material constant of the universal gas constant, and a proportionality constant. The material parameters for the above formulas are shown in Table 4. The increment in rotation rate induced by the pulse current is incorporated into each component of the grain orientation. Consequently, under PC conditions, equation (15) is modified as follows:

$$\Delta\varphi_i=\theta_0\cdot r_i\cdot\dot{\varepsilon}\cdot\Delta t+\dot{\varphi}(J)\Delta t,\quad where\ \ i=1,2,3 \tag{18}$$

Table 4 Parameters for modeling the grain rotation mechanism [60–62]

Thermal activation/ Q/(kJ/mol)	Atomic volume/Ω/(m^3)	Grain boundary thickness/δ	Boltzmann constant /k	Shear modulus /G/(MPa)	Burgers vector/ b/(m)	Poisson's ratio /v
135	15.5E-30	10E-9	1.38×10E-23	85246	2.86×10E-10	0.33

Effective valence /Z^*	Electron charge /e/(C)	Electrical resistivity/ ρ_e/(Ω·m)	Atomic density /N/(m^{-3})	Universal gas constant /R/(J/K/mol)	Proportionality constant /D_0 (m^2/s)
10	1.6E-19	1.11E-7	8.39E25	8.314	10E-3

5 Cellular automata modelling for grain refinement

5.1 Initial microstructure and setup of CA model

In the CA simulation technique, each CA cell represents a cluster of metal atoms with a specific grain orientation. The clusters are considered homogeneous, and therefore all physical parameters are set to homogeneous values. Figure 1(a) shows that the volume fraction of the phase composition of α-ferrite is dominant. In addition, the remaining lamellar pearlite is also composed of about 88% α-ferrite and 12% Fe_3C [63]. Therefore, it can be assumed that the volume of α-ferrite in the material is dominant. In this paper, the CA model is constructed as a single-phase polycrystalline material and temporarily ignores the influence of the difference in physical properties of the different phase compositions between pearlite and α-ferrite on the microscopic current distributions. The fundamental state of a cell is determined by the Euler angle (φ_1, ψ, φ_2), which is also the basic parameter that characterizes the microstructure in physical reality. The microstructure of the CA model with an average grain size of 14.7 μm obtained by the grain-grown algorithm is shown in Figure 12(a) [64]. The CA model for grain refinement is selected from a specific region, shown by the red rectangle. The texture of the annealed BCC metal is usually very weak [65], so a random set of Euler angles is assigned to the cells belonging to the same grain. The

CA model space taken for grain refinement is 400 × 400, and the size of each CA cell l_0 is 0.12 μm × 0.12 μm, which is consistent with the measurement step size of the EBSD tests. The current direction of the boundary conditions flows in from the left side of the model and out from the right side, while the deformation loading is applied from the top of the model. Their numerical magnitudes can be referred to Figure 4(c). Figure 12(b) shows that grain size distribution is consistent with the experimental results in Figure 1(b) with a relative error of 5%.

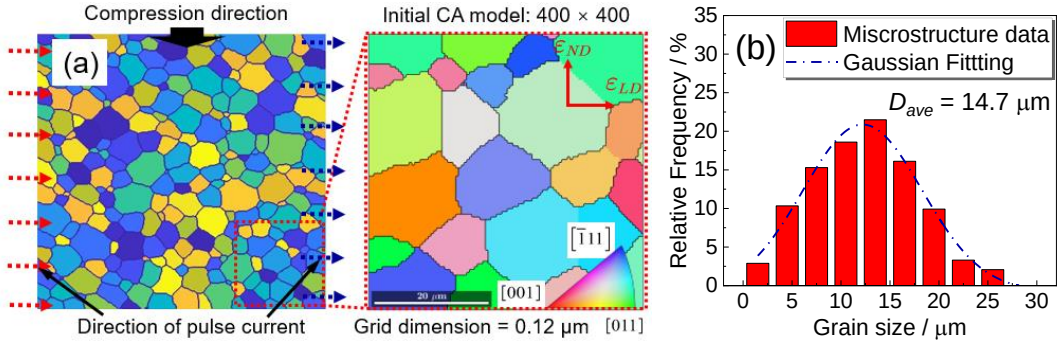

Fig. 12. Initial microstructure by a grain growth algorithm; (a) grain morphology and orientation and (b) grain size distribution

5.2 Topological deformation model

Under the compression conditions, the material will undergo reduction along the *ND* direction while extending along the *LD* direction. The relationship between the before and after deformation of the CA model can be related through the deformation gradient tensor *F*, i.e. [66]:

$$f_x = \partial x/\partial X;\quad f_y = \partial y/\partial Y; F = \begin{bmatrix} f_x & 0 \\ 0 & f_y \end{bmatrix} \tag{19}$$

where, the variables (*x*, *y*) represent the cell coordinates after deformation, and (*X*, *Y*) are the coordinates of the same cell before deformation, respectively. It is worth noting that plane strain compression only involves dimensional deformation in two dimensions, as the amount of deformation in the *Z*-direction is much smaller than in the other two directions. Therefore, *F* can be easily obtained from the plastic deformation volume invariance principle ($f_x = 1/f_y$) to calculate the deformation gradient for compressive deformation by using the following formula [22]:

$$\varepsilon_p = \begin{bmatrix} -\ln f_y & 0 \\ 0 & \ln f_y \end{bmatrix} \tag{20}$$

where, ε_p represents the plastic strain that the CA model undergoes. At this point, the quantitative relationship between the amount of plastic deformation and the amount of topological deformation of the grain morphology has been constructed. This allows the model to accurately characterize the influence of plastic deformation on the grain morphology (such as the aspect ratio) during the microstructure evolution.

5.3 Introduction of a discrete model to calculate the pulse current and temperature distribution

As is known, the microstructure of metal is considered a heterogeneous material due to the presence of two phases with different physical characteristics, namely grain interior and grain boundary. The heterogeneous physical feature leads to an inconsistent distribution of microscopic current density across different phases and locations, so that the intensity of the electron wind effect related to the current

density is also non-uniform [27,58,59]. The non-uniform distribution of the current density causes the dislocation density evolution and rotation rate of the grain orientation to be unequal in the whole CA space. It is essential to develop a microscopic current density calculation method for the CA model to investigate the non-uniform effect of the current density on the grain refinement process. The current density distribution of a continuous medium must satisfy Maxwell's governing equation, i.e.:

$$\nabla \cdot J = 0 \tag{21}$$

where J is the magnitude of the current density in a finite volume and can be calculated as follows:

$$J = \sigma_e \cdot E = -\sigma_e \cdot \nabla \Phi \tag{22}$$

where Φ is the electric potential value, and σ_e is the electrical conductivity of the material. Consequently, equation (22) is substituted into equation (21) to obtain the differential governing equation for electric potential value as:

$$\nabla \left(\sigma_e \cdot \nabla \Phi \right) = 0 \tag{23}$$

Corresponding to the discrete space of the CA model, the smallest unit is the cell, which is also set to possess a uniform physical parameter of electric potential $\Phi(x, y)$. The cell state transition of the CA model is considered to be only related to itself and its neighbors. For example, the grain growth model assumes that neighboring cells will determine whether they will be transformed into the same state as the central cell based on the grain growth rate formula, as shown in Figure 13(a). In natural physical processes, the growth of equiaxed grains should follow an arbitrary radial direction. However, it is simplified in the CA model to grow along the four directions of neighbors. Although this simplified model may result in a loss of model simulation accuracy, the error can be negligible when the cell space is relatively small. The direction of the electrical current flowing in or out of the finite volume is arbitrary. This study is similarly simplified to the four directions, as shown in Figure 13(b). A sufficiently small moving vector representing the direction of current flow can always be decomposed into two mutually perpendicular components, similar to the Lattice Boltzmann Method (LBM) in computational fluid dynamics [67]. By applying equation (23) to the discrete space of individual CA cells in Figure 13(b), it is easy to obtain that:

$$\sum_{\kappa=1}^{4} \left(\varphi_\kappa - \varphi_c \right) \cdot \sigma_{\kappa c} = 0 \tag{24}$$

where subscript c represents the position of the central cell (i, j), and the subscript κ represents the neighboring cells, namely (i-1, j), (i, j+1), (i+1, j) and (i, j-1), respectively. $\sigma_{\kappa c}$ is the electrical conductivity between the central cell and neighboring. Since the microstructure tends to accumulate dislocation density at the grain boundary phase, the atoms are relatively disordered near the grain boundary. The electrons will have greater resistance when passing through the grain boundaries. Therefore, the electrical conductivity at the grain interior σ_i is usually greater than that of the grain boundary σ_{GB}. Recent studies have shown that the contribution of the grain boundary effect to increase the electrical resistivity can exceed 50 %. Considering the small volume fraction of grain boundary in the microstructure, it predicts that the σ_i is significantly higher than σ_{GB}. According to the literature [68,69], the σ_i used for this study is 9.009×10^6 s/m, while the σ_{GB} is about 9.337×10^5 s/m. The value of the σ_{GB} is about 1/10 of the σ_i, in agreement with what is described in the literature [32].

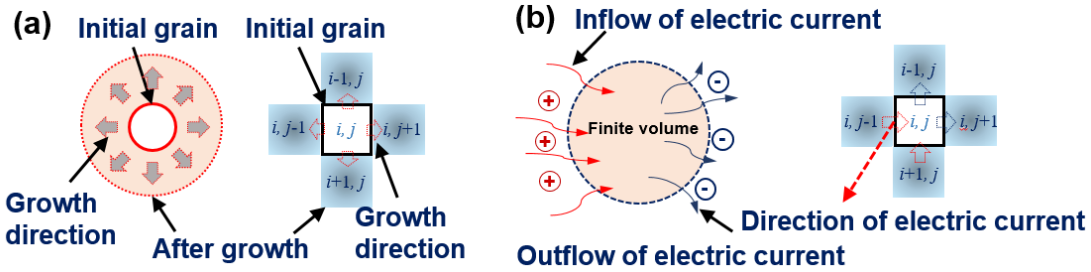

Fig. 13. The schematic diagram of (a) the grain growth model and (b) microscopic current density flow model under the Cellular neighborhood space

The temperature distribution of the whole CA model can be calculated based on the heat conduction control equation and Joule heat theory. Similarly, since the CA model has completed the spatial discretization, the value of the cell temperature increment ΔT at each computational step is expressed by the following differential equation [70]:

$$C_T \rho \Delta T = k_t \left(\frac{\partial^2 T}{\partial l_0^2} + \frac{\partial^2 T}{\partial l_0^2} \right) + Q_{Joule} \tag{25}$$

where, C_T and k_t are the specific heat capacity and thermal conductivity of 30CrMnSiA, respectively. Their values are obtained from Table 2. ρ is the material density of 7800 kg/m^3. Q_{Joule} is the heat source caused by the Joule heating effect. According to the literature[27], the Joule heat per unit volume equation can be expressed as $Q_{Joule} = J^2 / \sigma_e$. The value of σ_e depends on whether the central cell (i, j) is a grain boundary cell.

5.4 Summary of the CA algorithm and process

Figure 14 shows the simulation algorithm for the grain refinement. The model will be initialized first to ensure each cell is designated with a specific orientation. Furthermore, the evolution model parameters (strain rate, time step, total plastic strain, etc.) and material constants (electrical conductivity, thermal conductivity, density, etc.) are also set during the initialization module. In each simulated time step, the following procedure will be carried out. Firstly, the dislocation density for all cells in the CA model is updated based on the dislocation evolution model in section 4.1. Subsequently, the dislocation density variables are used to determine whether sub-grains are formed, and if so, the grain partition algorithm is executed. Otherwise, the existing sub-grain state is updated based on the dislocation density. The microstructure changes after forming new grains, so the current density and temperature distribution must be recalculated. Finally, the topological deformation module is carried out to update the spatial dimensions of the CA model based on the amount of plastic strain to capture the grain morphology changes.

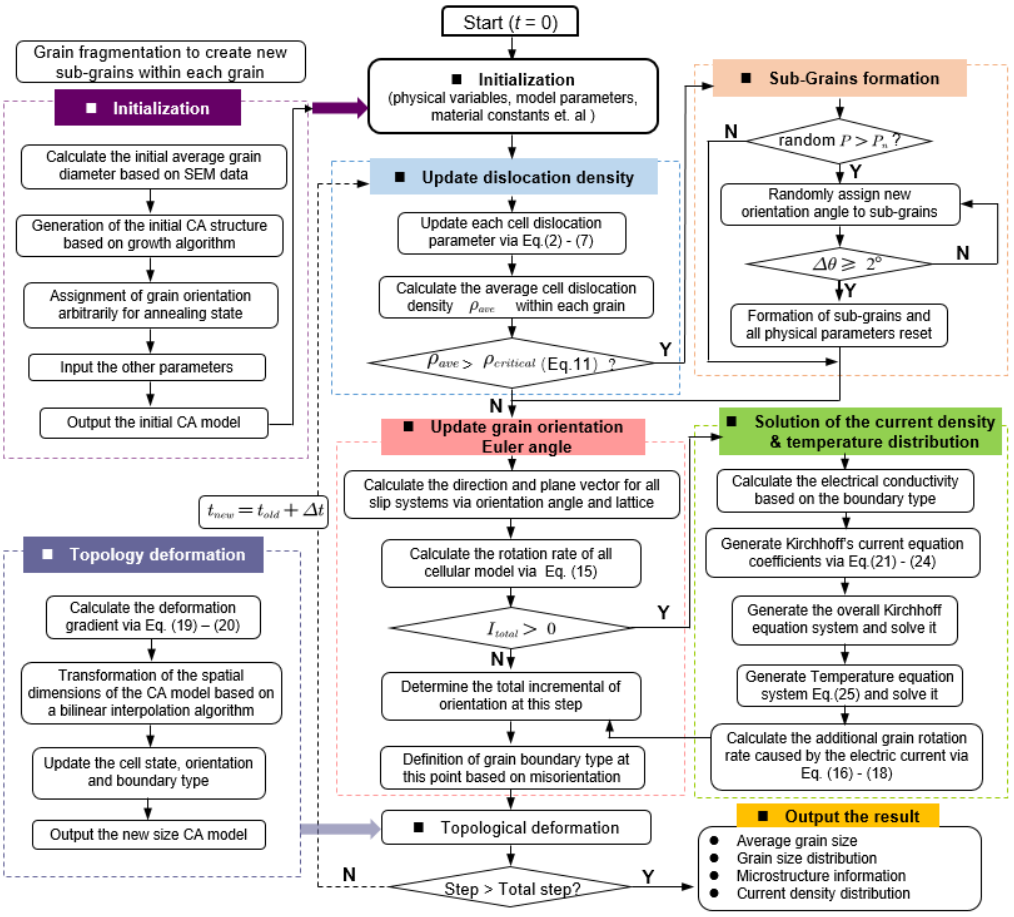

Fig. 14. The algorithm procedures for CA simulation for grain refinement with the pulse current effect

6 Simulation results and discussion

6.1 Results validation and analysis of CA model

Figure 15 shows the simulation results of the CA model under NC and PC conditions. As can be seen, the grain refinement constructed in this research accurately represents the evolution of the microstructure morphology. Since the model undergoes topological deformation of the grains due to plastic deformation, the theoretical grain aspect at the final stage should be close to the whole aspect ratio of the CA model (about 10 for length/width = 1320/120). However, due to the grain refinement, the aspect ratio of the final refined grains is still close to 1.0. The original equiaxed coarse grain is almost completely transformed into the same equiaxed refined microstructure with a large number of HAGBs, which is almost consistent with the result observed through the EBSD experiment in Figure 5. With the increase of strain, the grain size of the model gradually shifted from coarse grain to fine grain under both NC and PC conditions, which led to a gradual decrease of the equivalent grain size.

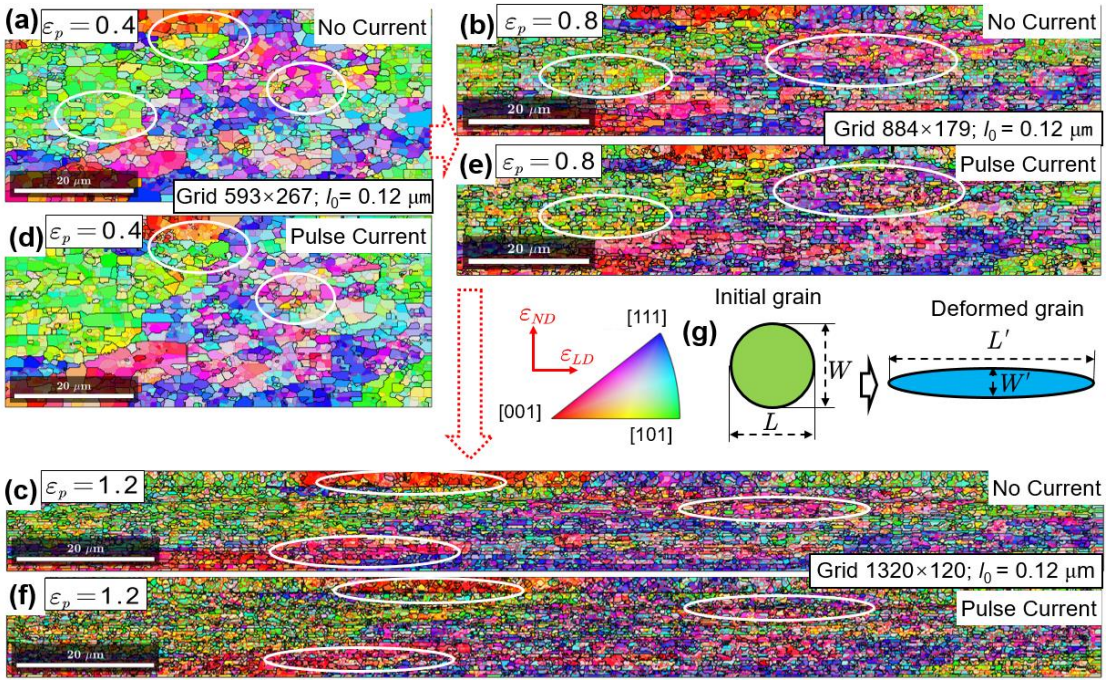

Fig. 15. Microstructure evolution under (a) NC & ε_p = 0.4; (b) NC & ε_p = 0.8; (c) NC & ε_p = 1.2; (d) PC & ε_p = 0.4; (e) PC & ε_p = 0.8; (f) PC & ε_p = 1.2 conditions and (g) schematic diagram of the grain topological deformation

The grain size distribution under NC and PC conditions at different conditions is shown in Figure 16. The results show that the grain size distribution has deviated from the Gaussian distribution after deformation and is consistent with the general result of some severe plastic deformation processes, such as shown in the literature [25]. With the increase of strain, the grain size of the model gradually shifted from coarse grain to refined grain (< 0.7 μm) under both NC and PC conditions, which led to a gradual decrease of the equivalent grain size, and the trend was also consistent with the EBSD results. The results from the CA model also show that the D_{eq} for ε_p = 0.4 - 1.2 is 5.32 μm, 4.32 μm, and 1.56 μm under NC conditions, and 4.79 μm, 3.14 μm, and 1.37 μm under PC conditions, respectively. The model exhibits a relative error of 10.48 % and 8.55 % for D_{eq} under NC and PC conditions at ε_p = 1.2, respectively. However, differences exist between the CA model results and the EBSD test, as seen in Figure 16(a) and Figure 16(d). Due to the high thermal conductivity of metals, even locally high temperatures caused by local high current density at grain boundaries will conduct to other regions and reach equilibrium quickly [32]. Therefore, the high current density at grain boundaries is the main reason for causing charge imbalance, alteration, and nucleation. This could be the mechanism through which low-temperature recrystallization occurs. In other words, low-temperature recrystallization induced by the pulsed currents described above may have happened in the tests. However, the CA model has not yet considered this mechanism. Consequently, the percentage of refined grains obtained from the model simulation at low strains may not align with the EBSD results. As the strain increases, the dominant mechanism of strain-induced grain refinement gradually takes precedence, thus reducing this discrepancy. The simulated results generally exhibit an acceptable error in predicting the microstructure evolution process during severe plastic deformation of 30CrMnSiA under NC and PC conditions, respectively.

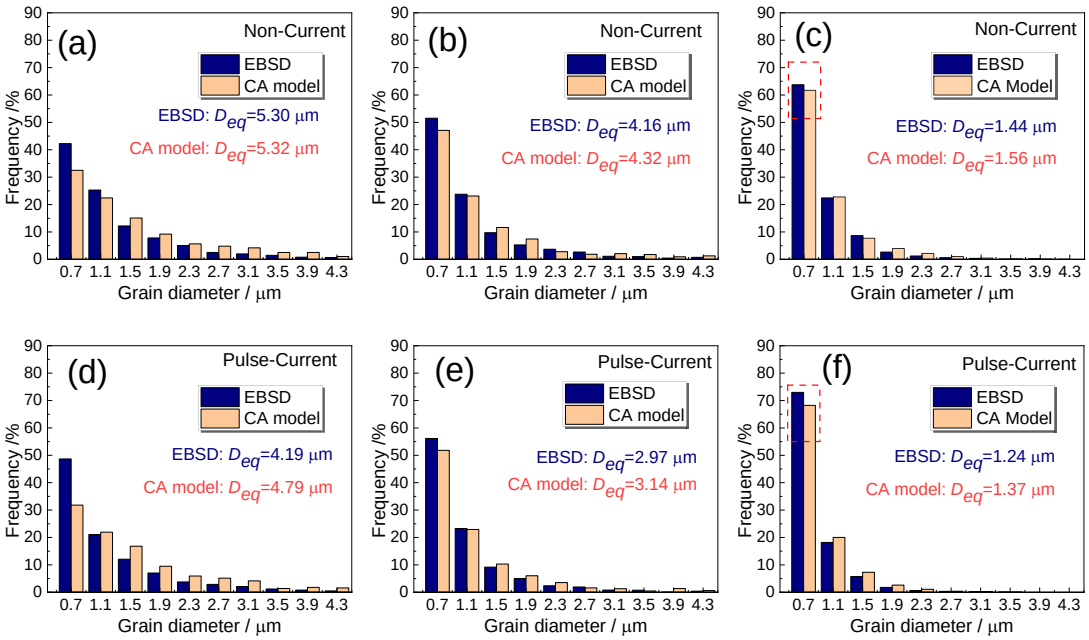

Fig. 16. Grain size distribution of CA and EBSD under (a) NC condition and ε_p = 0.4; (b) NC condition and ε_p = 0.8; (c) NC condition and ε_p = 1.2; (d) PC condition and ε_p = 0.4; (f) PC condition and ε_p = 0.8; (e) PC condition and ε_p = 1.2

6.2 Influence of pulse Current on grain refinement

In addition, comparing the NC and PC conditions at the same strain level, the result shows that the percentage of HAGBs and refined grain under the PC condition is more than that under the NC condition. Figure 15 shows the difference between NC and PC conditions in the same area marked with white circles. The percentage of refined grains (< 0.7 um) is higher in the PC condition than in the NC condition at the same strain level, as shown in Figure 16. For example, comparing the red square rectangle in Figure 16(c) and Figure 16(f), the percentage of refined grains is 72.96% in the PC condition compared to 63.74 % in the NC condition. CA simulation presents similar results; the percentage of fine grains is 68.23% in the PC condition, which is higher than 61.7% in the NC condition. The CA model, constructed based on the mechanism of accelerated grain rotation induced by pulsed current, accurately characterizes the transformation of LAGBs into HAGBs facilitated by the pulsed current. Thus, the pulse current-promoted grain refinement is also accurately characterized. The phenomenon of electroplasticity on grain refinement has been discovered in many studies [6,8]. However, there is still considerable controversy concerning the electroplastic effect. To investigate the effect of pulsed current on the grain refinement process, Figure 17 shows the temperature and current density distribution at various strains. The left side of the red dashed line of each subplot in Figure 17 represents the temperature distribution, while the right side represents the current density distribution. As a comparison, the current density distribution at the initial microstructure is also shown in Figure 17(a). Due to the different conductivity parameters at the grain boundaries and inside the grains, a considerable current density gradient occurs near the grain boundaries, especially at the nodes where multiple grain boundaries intersect. The red circles in the figure are high current density regions, which lead to low current density regions next to the high current densities, as shown in the white circle. Furthermore, similar to the literature [32], it is showed that the difference in local current density between grain boundaries and the grain interior does not lead to elevated temperatures exclusively at grain boundaries. Owing to the high thermal conductivity of the metal, the temperature distribution remains relatively uniform. It implies that the differences in pulse

current distribution under PC conditions may be the leading cause of the differences in microstructural evolution rather than the Joule heating effect.

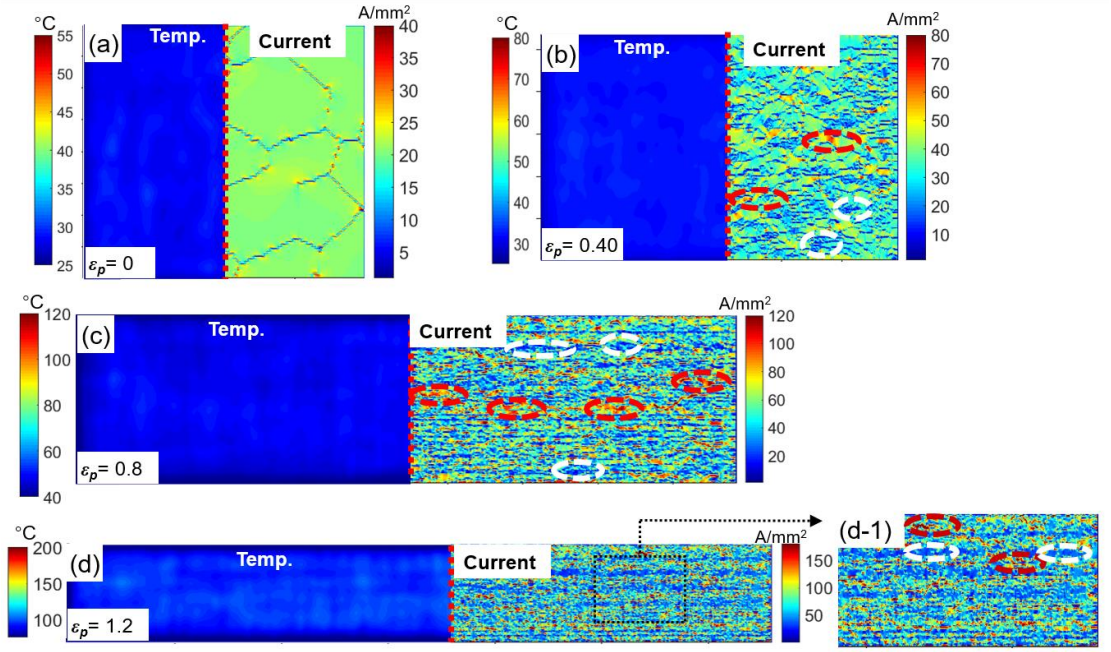

Fig. 17. Temperature & Electric current density maps of CA model varied with strain: (a) original, (b) ε_p = 0.4, (c) ε_p = 0.8 and (d) ε_p = 1.2 with enlarged image (d-1)

Figure 18 shows the percentage of current density under different strain conditions and the variation of the maximum current density, average current density, and minimum current density with strain. As can be seen from Figure 18(a), with the increase of strain, the average current density gradually moves away from x = 0, and the distribution forms from a single peak to a broadband bimodal morphology, representing a gradual increase in the degree of dispersion of current density distribution. As the plastic strain ε_p increases from 0 to 1.2, the average current density increases from 20.52A/mm^2 to 91.64 A/mm^2 with a 3.5-fold increase. The minimum current density increases from 2.9 A/mm^2 to 8.04 A/mm^2, similar to the fold increase in the average current density. However, the peak current density increased sharply from 53.31 A/mm^2 to 430.78 A/mm^2 with a 7-fold increase. These additional increases are due to the effects of grain refinement phenomena during microstructure evolution. Areas undergoing grain refinement possess a higher boundary proportion and resistance, redirecting a major portion of the current toward the coarser crystalline areas. Therefore, within the relatively coarse grains of the model space, a higher equivalent current density translates to a greater electroplastic effect, as showed by the red circles in Figure 17. It causes a further increase in the rotation rate of grain orientation based on equation (16) and then accelerates the formation of LAGBs and HAGBs in relatively coarse grains. Figure 18(b) also shows that the peak pulsed current density value increases rapidly with ongoing grain refinement. This can explain the observed increase in the difference between the NC and PC conditions as strain increases, as discussed in Section 3.

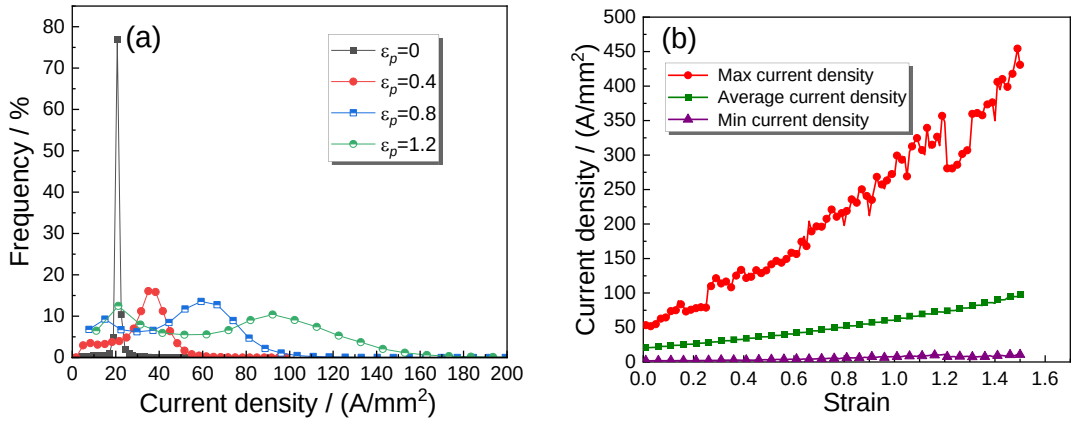

Fig. 18. Statistical value of electric current density: (a) current density distribution and (b) average value, max value and min value varied with strain of CA model

6.3 Effect of inhomogeneous current density on microstructural homogeneity

Compared to Figure 5(c) and Figure 15(c), the microstructure of the EBSD experiments (Figure 5(f)) and CA model calculations (Figure 15(f)) under PC conditions in the present study are more homogeneous. For instance, Figure 5(c) still shows the presence of coarse grains (blue circles), whereas Figure 5(f) exhibits no significant coarse grain component. Some researchers have attributed this phenomenon to DRX caused by the effect of pulse current [10,71]. Although the deformation temperatures are far from the conditions for high-temperature dynamic recrystallization, they believe that the pulse current may induce low-temperature dynamic recrystallization [23]. However, the simulation results obtained from the CA model constructed in this study offer an alternative explanation. The temperature distribution caused by pulsed current does not exhibit significant differences, indicating that the influence of pulsed currents is dominant. The schematic diagram of the mechanism by which pulse current affects grain refinement is shown in Figure 19. As strain increases, the chain-like refined grains will first be formed in the coarse grains exhibiting high dislocation density. The already refined grains will become low current-density regions in the next evolution step, which reduces the probability of continuing to refine the grains. However, if grain refinement did not occur at some region in the previous step, there is a large amount of sub-grain in the coarse grains, and the average pulse current within the grain is also higher. Then, a high current density will accelerate the grain rotation rate of the sub-grain in this region to form HAGBs (refer to equation (16)), promoting the grain refinement process. In other words, the inhomogeneity of the pulse current density reduces the difference in grain refinement rates at different regions of the CA model, thus helping to produce a uniformly refined microstructure.

6.4 Applicability and limitation of the CA model

The CAFS offers various advantages, including enhanced grain refinement, improved mechanical properties, and effective reduction of residual stress after deformation [71–73]. These benefits are closely tied to the mechanism of microstructure evolution. However, it is crucial to adjust the process and pulse current parameters carefully, as improper combinations may fail to sufficiently activate the electroplastic effect or result in excessive temperature elevation effects. The trial and error method is applicable for optimizing process and pulse current parameters in specific procedures like stamping and bending [74,75]. Because the current density through the blanks is constant, with a uniform cross-sectional area. However, it is essential to note that complex forming processes like spinning involve continuous changes in the topological geometry of the part, resulting in significant variations of current density. Employing a trial-and-error method to determine suitable process parameter combinations for such scenarios would result in substantial economic and time costs. The results and models from this study can be used in the

early stages of process development for the preparation of structural parts using the current-assisted spinning process. While this paper focuses on plane strain compression deformation, it is essential to note that the boundary conditions driving the constructed model are theoretically applicable to various deformation states and current densities. The model can also forecast grain size and its distribution across different locations of the part during the early stages of process design, which facilitates the development and adjustment of subsequent process parameters. In the future, it can also be used to build up a rich and reliable material database by carrying out many numerical experiments to realize the shape/property integration of the complex parts.

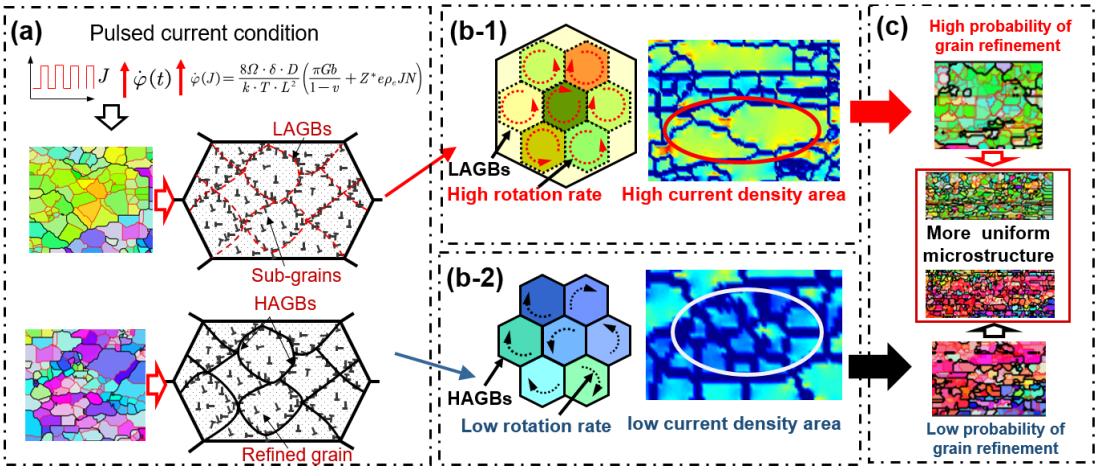

Fig. 19. Mechanism schematic of electroplastic effect on the grain refinement process at different regions: (a) summary of the grain refinement process, (b-1) high current density region, (b-2) low current density region and (c) refined grains

The CA model does not account for the influence of pulsed current on dislocation morphology, as understanding the mechanisms behind the electroplasticity effect still needs further study [49]. Consequently, the model cannot simulate the evolution of other microscopic parameters, such as the percentage of grain boundary types (LAGBs and HAGBs) and the texture strength. The study aims to investigate the mechanism of electrical current impact on microstructure evolution in the absence of significant thermal effects. However, the range of current parameters in current-assisted forming processes is extensive. For instance, as the increase of thinning rates during flow spinning processes or multi-pass rolling, the current density may exceed 100 A/mm^2. Consequently, the heating effect caused by the pulsed current becomes noticeable. A comprehensive CA model that considers electroplasticity should also include mechanisms such as dynamic recrystallization phenomena under high-temperature conditions. The CA model developed in this study does not consider the impact of variations in physical properties among different phases. The pearlite phase, as the hardening precipitation phase of the material, may also affect the grain refinement process. The construction of a multiphase polycrystalline CA model will be attempted in subsequent work to improve the accuracy further. Furthermore, utilizing two different computational software platforms, ABAQUS and MATLAB, for the FE and CA models, respectively, necessitates separate solving of the macro and micro models, thereby compromising computational efficiency.

7. Conclusion

In this study, the deformed samples of 30CrMnSiA under different strains were obtained using

CAPSC tests. The microstructure evolution mechanism was then investigated using the EBSD technique. Finally, a modified CA model incorporating the electroplastic effect was developed to analyze the mechanism of the electroplastic effect on grain refinement. According to the research results, the following conclusions can be obtained:

1. Strain-induced grain fragmentation is the main grain refinement mechanism during the CAPSC process. When $\varepsilon_p = 0.4$, the difference between the GOS_{mean} value and the area ratio of refined grains in the microstructure under NC and PC conditions is 2.8% and 1.72%, respectively. However, as the strain increases to $\varepsilon_p = 1.2$, the differences between NC and PC conditions expand to 24.24% and 15.53%, respectively. It shows that the greater the deformation, the larger the difference in grain refinement caused by the pulse current effect, indicating a complex interaction mechanism between pulse current and grain refinement.

2. Mathematical models of strain-induced dislocation density accumulation, sub-grain boundary generation, sub-grain deflection, and high-angle grain boundary formation during severe plastic deformation are constructed. A numerical algorithm for calculating the local current density distribution was introduced within the framework of the traditional CA model to take into account the mechanism of the pulse current effect on the microstructure evolution. The relative errors of the constructed CA model are 10.48 % and 8.55 % under NC and PC conditions, respectively. This proves that the model can effectively predict the microstructure evolution process caused by the coupling effect of the severe plastic deformation and electroplastic effect.

3. The CA model results show that due to the current aggregation effect, the current density is lower in the fine grain regions with higher grain boundary content and higher inside the coarse grains. This uneven current density distribution will accelerate the grain refinement in coarse grain while inhibiting the further refinement in refined grain, thus facilitating the acquisition of a relatively uniform microstructure. The degree of current density distribution inhomogeneity intensifies with increasing strain, amplifying the disparity in microstructure evolution between NC and PC conditions.

In summary, the conclusions show that the CA model constructed in this paper successfully reveals the interaction mechanism between the pulse current and the grain refinement process and provides a theoretical basis and practical numerical simulation tool for the microstructure property control of the parts during the CAFS. In future work, the computational efficiency and accuracy of the CA model will be further improved, and the model will be applied to the study of microstructure evolution of blanks in CAFS, such as multi-pass current-assisted spinning and rolling, etc.

Data availability

The data required to reproduce these findings cannot be shared at this time as the data also forms part of an ongoing study.

CRediT authorship contribution statement

Can Chen: Conceptualization, Methodology, Software, Validation, Formal analysis, Investigation, Data Curation, Writing - Original Draft, Visualization, Funding acquisition. **Qinxiang Xia:** Supervision, Conceptualization, Methodology, Validation, Investigation, Resources, Data Curation, Writing - Review & Editing, Visualization, Project administration, Funding acquisition. **Haoyang Zhou:** Validation, Data Curation. **Jie Zhao:** Validation, Data Curation. **Yi Qin:** Supervision, Validation, Resources, Writing - review & editing. **Gangfeng Xiao:** Conceptualization, Methodology.

Declaration of competing interest

The authors report no declarations of interest.

Acknowledgements

This work was financially supported by the National Natural Science Foundation of China (52175316), the Natural Science Foundation of Basic and Applied Basic Research of Guangdong Province (2021A1515011074), Guangzhou Science and Technology Planning Project (201804010135), and the Guangdong Province Key Laboratory of Precision Equipment and Manufacturing Technology (PEMT1202). One of the authors, Can Chen, would also like to acknowledge financial support from the China Scholarship Council (No. 202106150053), which enabled him to conduct the research at the University of Strathclyde, UK.

References

[1] D.S. Svyetlichnyy, J. Majta, R. Kuziak, K. Muszka, Experimental and modelling study of the grain refinement of Fe-30wt%Ni-Nb austenite model alloy subjected to severe plastic deformation process, Arch. Civ. Mech. Eng. 21 (2021) 20. https://doi.org/10.1007/s43452-021-00178-7.

[2] J. Majta, Ł. Madej, D.S. Svyetlichnyy, K. Perzyński, M. Kwiecień, K. Muszka, Modeling of the inhomogeneity of grain refinement during combined metal forming process by finite element and cellular automata methods, Mater. Sci. Eng. A 671 (2016) 204–213. https://doi.org/10.1016/j.msea.2016.06.052.

[3] J.A. Muñoz, R.E. Bolmaro, A.M. Jorge, A. Zhilyaev, J.M. Cabrera, Prediction of Generation of High- and Low-Angle Grain Boundaries (HAGB and LAGB) During Severe Plastic Deformation, Metall. Mater. Trans. A 51 (2020) 4674–4684. https://doi.org/10.1007/s11661-020-05873-3.

[4] H.-D. Nguyen-Tran, H.-S. Oh, S.-T. Hong, H.N. Han, J. Cao, S.-H. Ahn, D.-M. Chun, A review of electrically-assisted manufacturing, Int. J. Precis. Eng. Manuf.-Green Technol. 2 (2015) 365–376. https://doi.org/10.1007/s40684-015-0045-4.

[5] C. Wu, Y. jie Zhou, B. Liu, Experimental and simulated investigation of the deformation behavior and microstructural evolution of Ti6554 titanium alloy during an electropulsing-assisted microtension process, Mater. Sci. Eng. A 838 (2022) 142745. https://doi.org/10.1016/j.msea.2022.142745.

[6] J. Zhang, Z. Liu, J. Sun, H. Zhao, Q. Shi, D. Ma, Microstructure and mechanical property of electropulsing tempered ultrafine grained 42CrMo steel, Mater. Sci. Eng. A 782 (2020) 139213. https://doi.org/10.1016/j.msea.2020.139213.

[7] M. Mei, Y. Song, J. Lu, H. Chuanchuan, X. Lechun, Modeling dynamic recrystallization behavior of Al-Zn-Mg-Cu alloy during electroshock assisted tension based on cellular automata, Mater. Res. Express 9 (2022) 036513. https://doi.org/10.1088/2053-1591/ac5e23.

[8] M. Du, B. Meng, Y.Z. Liu, F. Pan, M. Wan, Flow characteristics and microstructural evolution in pulsed current assisted micro-scaled compression of stainless steel sheet, J. Mater. Res. Technol. 15 (2021) 4397–4414. https://doi.org/10.1016/j.jmrt.2021.10.076.

[9] X. Li, X. Li, J. Zhu, X. Ye, G. Tang, Microstructure and texture evolution of cold-rolled Mg-3Al-1Zn alloy by electropulse treatment stimulating recrystallization, Scr. Mater. 112 (2016) 23–27. https://doi.org/10.1016/j.scriptamat.2015.09.001.

[10] T. Wang, X. Wei, H. Zhang, Z. Ren, B. Gao, J. Han, L. Bian, Plastic deformation mechanism transition with solute segregation and precipitation of 304 stainless steel foil induced by pulse current, Mater. Sci. Eng. A 840 (2022) 142899. https://doi.org/10.1016/j.msea.2022.142899.

[11] R. Teimouri, S. Skoczypiec, Simulation of gradient grain size and hardness in ultrasonic burnishing process through multi-physics of contact mechanic and microstructure evolution, Mech. Mater. 174 (2022) 104463. https://doi.org/10.1016/j.mechmat.2022.104463.

[12] S.F. Chen, D.Y. Li, S.H. Zhang, H.N. Han, H.W. Lee, M.G. Lee, Modelling continuous dynamic recrystallization of aluminum alloys based on the polycrystal plasticity approach, Int. J. Plast. 131 (2020) 102710. https://doi.org/10.1016/j.ijplas.2020.102710.

[13] F. Khodabakhshi, H.A. Derazkola, A.P. Gerlich, Monte Carlo simulation of grain refinement during friction stir processing, J. Mater. Sci. 55 (2020) 13438–13456. https://doi.org/10.1007/s10853-020-04963-2.

[14] K.M. Min, W. Jeong, S.H. Hong, C.A. Lee, P.-R. Cha, H.N. Han, M.-G. Lee, Integrated crystal plasticity and phase field model for prediction of recrystallization texture and anisotropic mechanical properties of cold-rolled ultra-low carbon steels, Int. J. Plast. 127 (2020) 102644. https://doi.org/10.1016/j.ijplas.2019.102644.

[15] X. Xu, J. Zhang, J. Outeiro, B. Xu, W. Zhao, Multiscale simulation of grain refinement induced by dynamic recrystallization of Ti6Al4V alloy during high speed machining, J. Mater. Process. Technol. 286 (2020) 116834. https://doi.org/10.1016/j.jmatprotec.2020.116834.

[16] Y.-X. Liu, Y.C. Lin, Y. Zhou, 2D cellular automaton simulation of hot deformation behavior in a Ni-based superalloy under varying thermal-mechanical conditions, Mater. Sci. Eng. A 691 (2017) 88–99. https://doi.org/10.1016/j.msea.2017.03.039.

[17] P. Guo, L. Deng, X. Wang, J. Li, Modelling of dynamic recrystallization kinetics of 300M steel at high strain rates during hot deformation, Sci. China Technol. Sci. 62 (2019) 1534–1544. https://doi.org/10.1007/s11431-018-9412-1.

[18] Ł. Łach, J. Nowak, D. Svyetlichnyy, The evolution of the microstructure in AISI 304L stainless steel during the flat rolling – modeling by frontal cellular automata and verification, J. Mater. Process. Technol. 255 (2018) 488–499. https://doi.org/10.1016/j.jmatprotec.2017.12.001.

[19] D.-D. Chen, Y.C. Lin, F. Wu, A design framework for optimizing forming processing parameters based on matrix cellular automaton and neural network-based model predictive control methods, Appl. Math. Model. 76 (2019) 918–937. https://doi.org/10.1016/j.apm.2019.07.023.

[20] J. Long, N. Zhu, Q. Xia, X. Cheng, A Study of the Dynamic Recrystallization Behavior of Ni-Based Superalloy during Hot Power Spinning Based on Cellular Automaton, Adv. Eng. Mater. 21 (2019) 1801022. https://doi.org/10.1002/adem.201801022.

[21] T. Sakai, A. Belyakov, R. Kaibyshev, H. Miura, J.J. Jonas, Dynamic and post-dynamic recrystallization under hot, cold and severe plastic deformation conditions, Prog. Mater. Sci. 60 (2014) 130–207. https://doi.org/10.1016/j.pmatsci.2013.09.002.

[22] L. Liu, Y. Wu, A.S. Ahmad, A novel simulation of continuous dynamic recrystallization process for 2219 aluminium alloy using cellular automata technique, Mater. Sci. Eng. A 815 (2021) 141256. https://doi.org/10.1016/j.msea.2021.141256.

[23] F. Yin, S. Ma, S. Hu, Y. Liu, L. Hua, G.J. Cheng, Understanding the microstructure evolution and mechanical behavior of titanium alloy during electrically assisted plastic deformation process, Mater. Sci. Eng. A 869 (2023) 144815. https://doi.org/10.1016/j.msea.2023.144815.

[24] K.K. Alaneme, E.A. Okotete, Recrystallization mechanisms and microstructure development in

emerging metallic materials: A review, J. Sci. Adv. Mater. Devices 4 (2019) 19–33. https://doi.org/10.1016/j.jsamd.2018.12.007.

[25] J. Zhang, X. Xu, J. Outeiro, H. Liu, W. Zhao, Simulation of Grain Refinement Induced by High-Speed Machining of OFHC Copper Using Cellular Automata Method, J. Manuf. Sci. Eng. 142 (2020). https://doi.org/10.1115/1.4047431.

[26] G. Liu, D. Zhang, C. Yao, Investigation of the grain refinement mechanism in machining Ti-6Al-4V: Experiments and simulations, J. Manuf. Process. 94 (2023) 479–496. https://doi.org/10.1016/j.jmapro.2023.03.077.

[27] J. Zhao, G.-X. Wang, Y. Dong, C. Ye, Multiscale modeling of localized resistive heating in nanocrystalline metals subjected to electropulsing, J. Appl. Phys. 122 (2017) 085101. https://doi.org/10.1063/1.4998938.

[28] Q. Xia, C. Chen, G. Xiao, K. Chen, H. Zhou, A modified dislocation density-based model of 30CrMnSiA considering the coupling effect of electroplasticity and grain refinement during the pulsed current-assisted plane strain deformation, J. Mater. Sci. (2023). https://doi.org/10.1007/s10853-023-08792-x.

[29] Q.X. Xia, C. Chen, G.F. Xiao, H.Y. Zhou, Research on flow behavior of 30CrMnSiA during current-assisted plane strain compression deformation, IOP Conf. Ser. Mater. Sci. Eng. 1270 (2022) 012003. https://doi.org/10.1088/1757-899X/1270/1/012003.

[30] D.F. Barbin, L.C. Neves Filho, V. Silveira, Convective heat transfer coefficients evaluation for a portable forced air tunnel, Appl. Therm. Eng. 30 (2010) 229–233. https://doi.org/10.1016/j.applthermaleng.2009.08.009.

[31] K. Yu, F. Zhang, D. Liu, Y. Liu, Spectral emissivity of type E235B low carbon structural steel with different roughnesses, Opt. Rev. 24 (2017) 540–548. https://doi.org/10.1007/s10043-017-0345-8.

[32] M.-J. Kim, S. Yoon, S. Park, H.-J. Jeong, J.-W. Park, K. Kim, J. Jo, T. Heo, S.-T. Hong, S.H. Cho, Y.-K. Kwon, I.-S. Choi, M. Kim, H.N. Han, Elucidating the origin of electroplasticity in metallic materials, Appl. Mater. Today 21 (2020) 100874. https://doi.org/10.1016/j.apmt.2020.100874.

[33] T. Wang, B. Yu, Y. Wang, S. Jiang, Effect of beam current on microstructures and mechanical properties of joints of TZM/30CrMnSiA by electron beam welding, Chin. J. Aeronaut. 34 (2021) 122–130. https://doi.org/10.1016/j.cja.2020.05.031.

[34] M. Rout, R. Ranjan, S.K. Pal, S.B. Singh, EBSD study of microstructure evolution during axisymmetric hot compression of 304LN stainless steel, Mater. Sci. Eng. A 711 (2018) 378–388. https://doi.org/10.1016/j.msea.2017.11.059.

[35] K.P. Mingard, B. Roebuck, E.G. Bennett, M.G. Gee, H. Nordenstrom, G. Sweetman, P. Chan, Comparison of EBSD and conventional methods of grain size measurement of hardmetals, Int. J. Refract. Met. Hard Mater. 27 (2009) 213–223. https://doi.org/10.1016/j.ijrmhm.2008.06.009.

[36] A. Hadadzadeh, F. Mokdad, M.A. Wells, D.L. Chen, A new grain orientation spread approach to analyze the dynamic recrystallization behavior of a cast-homogenized Mg-Zn-Zr alloy using electron backscattered diffraction, Mater. Sci. Eng. A 709 (2018) 285–289. https://doi.org/10.1016/j.msea.2017.10.062.

[37] J. Gao, H. Li, X. Sun, X. Zhang, M. Zhan, Electro-thermal-mechanical coupled crystal plasticity modeling of Ni-based superalloy during electrically assisted deformation, Int. J. Plast. 157 (2022) 103397. https://doi.org/10.1016/j.ijplas.2022.103397.

[38] A. Azizi, H.R. Abedi, Room temperature compressive superplasticity of low density steel, Scr.

Mater. 216 (2022) 114757. https://doi.org/10.1016/j.scriptamat.2022.114757.

[39] M. Bacca, D.R. Hayhurst, R.M. McMeeking, Continuous dynamic recrystallization during severe plastic deformation, Mech. Mater. 90 (2015) 148–156. https://doi.org/10.1016/j.mechmat.2015.05.008.

[40] X. Dong, Y.C. Shin, Predictive modeling of microstructure evolution within multi-phase steels during rolling processes, Int. J. Mech. Sci. 150 (2019) 576–583. https://doi.org/10.1016/j.ijmecsci.2018.10.061.

[41] C. Wang, X. Hu, Y. Cheng, X. Wang, H. Deng, S. Wang, S. Yao, Experimental investigation and numerical study on ultrasonic impact treatment of pure copper, Surf. Coat. Technol. 428 (2021) 127889. https://doi.org/10.1016/j.surfcoat.2021.127889.

[42] Y. Estrin, L.S. Tóth, A. Molinari, Y. Bréchet, A dislocation-based model for all hardening stages in large strain deformation, Acta Mater. 46 (1998) 5509–5522. https://doi.org/10.1016/S1359-6454(98)00196-7.

[43] Y. Estrin, H.S. Kim, Modelling microstructure evolution toward ultrafine crystallinity produced by severe plastic deformation, J. Mater. Sci. 42 (2007) 1512–1516. https://doi.org/10.1007/s10853-006-1282-2.

[44] H. Ding, N. Shen, Y.C. Shin, Modeling of grain refinement in aluminum and copper subjected to cutting, Comput. Mater. Sci. 50 (2011) 3016–3025. https://doi.org/10.1016/j.commatsci.2011.05.020.

[45] H. Ding, N. Shen, Y.C. Shin, Predictive modeling of grain refinement during multi-pass cold rolling, J. Mater. Process. Technol. 212 (2012) 1003–1013. https://doi.org/10.1016/j.jmatprotec.2011.12.005.

[46] J. Tiwari, H. Krishnaswamy, M. Amirthalingam, Modelling Transient Mechanical Behavior of Aluminum Alloy During Electric-Assisted Forming, in: K. Inal, J. Levesque, M. Worswick, C. Butcher (Eds.), NUMISHEET 2022, Springer International Publishing, Cham, 2022: pp. 105–113. https://doi.org/10.1007/978-3-031-06212-4_10.

[47] M.-J. Kim, M.-G. Lee, K. Hariharan, S.-T. Hong, I.-S. Choi, D. Kim, K.H. Oh, H.N. Han, Electric current–assisted deformation behavior of Al-Mg-Si alloy under uniaxial tension, Int. J. Plast. 94 (2017) 148–170. https://doi.org/10.1016/j.ijplas.2016.09.010.

[48] Y.C. Zhao, M. Wan, B. Meng, J. Xu, D.B. Shan, Pulsed current assisted forming of ultrathin superalloy sheet: Experimentation and modelling, Mater. Sci. Eng. A 767 (2019) 138412. https://doi.org/10.1016/j.msea.2019.138412.

[49] Z. Xu, T. Jiang, J. Huang, L. Peng, X. Lai, M.W. Fu, Electroplasticity in electrically-assisted forming: Process phenomena, performances and modelling, Int. J. Mach. Tools Manuf. 175 (2022) 103871. https://doi.org/10.1016/j.ijmachtools.2022.103871.

[50] Y.Z. Liu, M. Wan, B. Meng, Multiscale modeling of coupling mechanisms in electrically assisted deformation of ultrathin sheets: An example on a nickel-based superalloy, Int. J. Mach. Tools Manuf. 162 (2021) 103689. https://doi.org/10.1016/j.ijmachtools.2021.103689.

[51] Z.C. Sun, H.L. Wu, J. Cao, Z.K. Yin, Modeling of continuous dynamic recrystallization of Al-Zn-Cu-Mg alloy during hot deformation based on the internal-state-variable (ISV) method, Int. J. Plast. 106 (2018) 73–87. https://doi.org/10.1016/j.ijplas.2018.03.002.

[52] L.S. Toth, C. Gu, Ultrafine-grain metals by severe plastic deformation, Mater. Charact. 92 (2014) 1–14. https://doi.org/10.1016/j.matchar.2014.02.003.

[53] L.S. Tóth, Y. Estrin, R. Lapovok, C. Gu, A model of grain fragmentation based on lattice curvature,

Acta Mater. 58 (2010) 1782–1794. https://doi.org/10.1016/j.actamat.2009.11.020.

[54] H. Zhu, F. Chen, H. Zhang, Z. Cui, Review on modeling and simulation of microstructure evolution during dynamic recrystallization using cellular automaton method, Sci. China Technol. Sci. 63 (2020) 357–396. https://doi.org/10.1007/s11431-019-9548-x.

[55] M. Salvini, N. Grilli, E. Demir, S. He, T. Martin, P. Flewitt, M. Mostafavi, C. Truman, D. Knowles, Effect of grain boundary misorientation and carbide precipitation on damage initiation: A coupled crystal plasticity and phase field *damage* study, Int. J. Plast. 172 (2024) 103854. https://doi.org/10.1016/j.ijplas.2023.103854.

[56] M. Azarbarmas, M. Aghaie-Khafri, A New Cellular Automaton Method Coupled with a Rate-dependent (CARD) Model for Predicting Dynamic Recrystallization Behavior, Metall. Mater. Trans. A 49 (2018) 1916–1930. https://doi.org/10.1007/s11661-018-4533-3.

[57] D.S. Svyetlichnyy, K. Muszka, J. Majta, Three-dimensional frontal cellular automata modeling of the grain refinement during severe plastic deformation of microalloyed steel, Comput. Mater. Sci. 102 (2015) 159–166. https://doi.org/10.1016/j.commatsci.2015.02.034.

[58] D. Waryoba, Z. Islam, B. Wang, A. Haque, Recrystallization mechanisms of Zircaloy-4 alloy annealed by electric current, J. Alloys Compd. 820 (2020) 153409. https://doi.org/10.1016/j.jallcom.2019.153409.

[59] J. Zhao, Z. Ren, H. Zhang, G.-X. Wang, Y. Dong, C. Ye, Electroplasticity in AZ31B subjected to short-duration high-frequency pulsed current, J. Appl. Phys. 125 (2019) 185104. https://doi.org/10.1063/1.5087465.

[60] A.J. Haslam, S.R. Phillpot, D. Wolf, D. Moldovan, H. Gleiter, Mechanisms of grain growth in nanocrystalline fcc metals by molecular-dynamics simulation, Mater. Sci. Eng. A 318 (2001) 293–312. https://doi.org/10.1016/S0921-5093(01)01266-7.

[61] K.E. Harris, V.V. Singh, A.H. King, Grain rotation in thin films of gold, Acta Mater. 46 (1998) 2623–2633. https://doi.org/10.1016/S1359-6454(97)00467-9.

[62] Y. Jiang, G. Tang, C. Shek, J. Xie, Z. Xu, Z. Zhang, Mechanism of electropulsing induced recrystallization in a cold-rolled Mg–9Al–1Zn alloy, J. Alloys Compd. 536 (2012) 94–105. https://doi.org/10.1016/j.jallcom.2012.05.014.

[63] E. Gadalińska, A. Baczmański, C. Braham, G. Gonzalez, H. Sidhom, S. Wroński, T. Buslaps, K. Wierzbanowski, Stress localisation in lamellar cementite and ferrite during elastoplastic deformation of pearlitic steel studied using diffraction and modelling, Int. J. Plast. 127 (2020) 102651. https://doi.org/10.1016/j.ijplas.2019.102651.

[64] D. Panda, R. Kushwaha, R.K. Sabat, S. Suwas, S.K. Sahoo, Microstructure and texture evolution during grain growth of AM30 magnesium alloy, Philos. Mag. 102 (2022) 2207–2233. https://doi.org/10.1080/14786435.2022.2102263.

[65] M. Adhikary, A. Chakraborty, A. Das, V. T, R.K. B, Influence of annealing texture on dynamic tensile deformation characteristics of Dual phase steel, Mater. Sci. Eng. A 736 (2018) 209–218. https://doi.org/10.1016/j.msea.2018.08.103.

[66] J. Wang, G. Chen, S. Huang, H. Zhang, Q. Chen, C. Zhang, Z. Du, Multi-scale modeling and simulation for multi-pass processing of Ta-2.5 W alloy, Int. J. Mech. Sci. 218 (2022) 107069. https://doi.org/10.1016/j.ijmecsci.2022.107069.

[67] K.J. Petersen, J.R. Brinkerhoff, On the lattice Boltzmann method and its application to turbulent, multiphase flows of various fluids including cryogens: A review, Phys. Fluids 33 (2021) 041302. https://doi.org/10.1063/5.0046938.

[68] F. Khodabakhshi, M. Kazeminezhad, The effect of constrained groove pressing on grain size, dislocation density and electrical resistivity of low carbon steel, Mater. Des. 32 (2011) 3280–3286. https://doi.org/10.1016/j.matdes.2011.02.032.

[69] L. Zhou, C. Davis, P. Kok, Steel microstructure – Magnetic permeability modelling: The effect of ferrite grain size and phase fraction, J. Magn. Magn. Mater. 519 (2021) 167439. https://doi.org/10.1016/j.jmmm.2020.167439.

[70] D. Tong, X. Yi, F. Tan, Y. Jiao, J. Liang, Three-dimensional numerical manifold method for heat conduction problems with a simplex integral on the boundary, Sci. China Technol. Sci. 67 (2024) 1007–1022. https://doi.org/10.1007/s11431-022-2321-9.

[71] K. Huang, C. Cayron, R.E. Logé, The surprising influence of continuous alternating electric current on recrystallization behaviour of a cold-rolled Aluminium alloy, Mater. Charact. 129 (2017) 121–126. https://doi.org/10.1016/j.matchar.2017.04.036.

[72] D. Ao, J. Gao, X. Chu, S. Lin, J. Lin, Formability and deformation mechanism of Ti-6Al-4V sheet under electropulsing assisted incremental forming, Int. J. Solids Struct. 202 (2020) 357–367. https://doi.org/10.1016/j.ijsolstr.2020.06.028.

[73] S. Xie, J. Zhang, R. Li, T. Yuan, M. Zhang, M. Wang, Z. Zhang, S. Deng, Q. Li, Accelerated precipitation of the B2 particles and its effect on Al0.3CoCrFeNi high-entropy alloy by electric current assisted annealing, Mater. Charact. 181 (2021) 111434. https://doi.org/10.1016/j.matchar.2021.111434.

[74] X.-R. Chu, L. Wang, S.-X. Lin, Z.-M. Yue, J. Gao, Experimental Investigation on Formability of AZ31B Magnesium Alloy V-Bending Under Pulse Current, Acta Metall. Sin. Engl. Lett. 31 (2018) 1249–1257. https://doi.org/10.1007/s40195-018-0734-4.

[75] D. Ao, X. Chu, J. Gao, Y. Yang, S. Lin, Experimental investigation on the deformation behaviors of Ti-6Al-4V sheet in electropulsing-assisted incremental forming, Int. J. Adv. Manuf. Technol. 104 (2019) 4243–4254. https://doi.org/10.1007/s00170-019-04133-y.